Mostafa Borji, BSc

Master Thesis 2017 supervised by:
Prof. Holger OTT
Dr. Torsten CLEMENS

Alkali-based Displacement Processes in Microfluidic Experiments: Application to the Matzen Oil Field

DEPARTMENT PETROLEUM ENGINEERING

MONTAN UNIVERSITÄT

To my parents

AFFIDAVIT

I declare in lieu of oath, that I wrote this thesis and performed the associated research myself, using only literature cited in this volume.

EIDESSTATTLICHE ERKLÄRUNG

Ich erkläre an Eides statt, dass ich diese Arbeit selbständig verfasst, andere als die angegebenen Quellen und Hilfsmittel nicht benutzt und mich auch sonst keiner unerlaubten Hilfsmittel bedient habe.

_____

Mostafa Borji, 21 September 2017

Acknowledgements

I would like to express my sincere gratitude to my advisor Prof. Holger Ott for the continuous support of my master thesis, for his patience, motivation, immense knowledge and for providing me the opportunity to do this research.

I respect and thank Dr. Torsten Clemens and Dr. Martin Ferno for their valuable comments and support.

My sincere thanks also goes to Dr. Jean Kormann, Dr. Siroos Azizmohammadi and Dr. Mohammad Sedaghat for their precious advice and guidance in my thesis.

I would also like to thank DI Kata Kurgyis, Peter Kronberger, and all my friends and lab mates for the motivational discussion and encouragement.

Last but by no means least; I am grateful to my family for their thorough support and help throughout my master studies and my whole life.

Abstract

The Austrian Matzen oil field is producing under waterflooding since more than 50 years. By waterflooding, in average 35% of the oil can be recovered. This means that the majority of the oil stays behind after applying conventional production methods, i.e. after primary and secondary production stages. It is also safe to assume that a large portion of hydrocarbons in the Matzen field cannot be produced further using secondary oil recovery methods. Tertiary methods, also called enhanced oil recovery (EOR), comprise techniques that aim to increase the recovery by targeting unrecovered trapped oil at the end of conventional production. Chemical flooding is one of these EOR techniques, which include the injection of alkali, surfactants and a variety of their combination. Alkaline flooding is believed to be the cheapest chemical EOR method and OMV is showing a growing interest in employing it in the Matzen field.

In this thesis, glass microfluidic devices (micromodels) are implemented to study pore-level alkaline-flooding mechanisms and their interactions with Matzen oil-field samples. Furthermore, microchips preparation and cleaning procedures have been developed and are proposed in the frame of the present thesis.

The experiments have been performed using the two most common alkali types; aqueous solutions with different concentrations of sodium hydroxide and sodium carbonate were injected into microchips, saturated with high TAN oil samples, supplied by OMV from Matzen (8th TH and 16th TH reservoirs). Likewise, a sample from the Flysh reservoir, which has a low TAN has been used to investigate the importance of petroleum acid constituents. The injection experiments were performed in secondary and tertiary recovery modes.

The Flysh oil sample showed the highest recovery in pure-waterflood experiments, likely because of a more favorable mobility ratio. In this case, no recovery enhancement was detected by injecting alkaline solutions. On the other hand, higher recoveries were recorded in alkaline flooding experiments using high TAN oil samples. The injection of sodium carbonate solution was much more efficient compared to sodium hydroxide. Furthermore, water in oil (W/O) and oil in water (O/W) emulsions were observed depending on the solution concentration and oil type. Large oil-water interfaces and oil threads were noticed as a sign of low interfacial tension.

Finally, experiments indicated higher overall oil recovery in secondary injection scenarios in comparison to conventional waterflooding and subsequent tertiary alkaline floods.

Zusammenfassung

Die Ölroduktion des Matzen Felds im Wiener Becken wird seit über 50 Jahren durch Wasserflutung aufrechterhalten. Generell erreicht man im Durchschnitt nach primärer Ölförderung und Wasserflutung eine kumulative Förderung von etwa 35% des im Reservoir vorhandenen Öls – eine erhebliche Menge an Öl verbleibt also in der Lagerstätte. Auch für das Matzen Feld gilt, dass eine beträchtliche Menge an Öl auch durch sekundäre Ölgewinnung nicht produziert werden kann und man zu tertiären Methoden greifen muss. Unter tertiärer Ölgewinnung (Enhanced Oil Recovery oder EOR) versteht man verschiedene Techniken die nach der sekundären Ölgewinnung eingesetzt werden, und die über die Aufrechterhaltung des Lagerstättendrucks und einfachen Verdrängungsmechanismen hinausgehen, mit dem Ziel, die Gewinnung der nicht förderbaren Mengen nach konventioneller Produktion zu steigern.

Chemical EOR umfasst einen Bereich dieser tertiären Methoden, in dem Tenside zum Einsatz kommen um einen höheren Entölungsgrad zu erreichen. Mittels Alkaline Flooding könne diese Tenside in-situ aus dem Rohöl gewonnen werden. Alkaline Flooding gilt derzeit als kostengünstigste chemical-EOR Methode. Deshalb, und wegen der Zusammensetzung des Öls, hat die OMV ein gesteigertes Interesse diese Methode im Matzen Ölfeld anzuwenden.

In der vorliegenden Arbeit wird Mikrofluidik (sogenannte Mikromodelle) angewandt um die Verdrängungseffizienz mittels alkalischer Lösungen zu bestimmen. Die Experimente werden mit verschiedenen Rohöl Proben des Matzen Felds durchgeführt. Darüber hinaus wurden im Rahmen der vorliegenden Arbeit Probenpräparations- und Reinigungsverfahren entwickelt und getestet.

Für die Experimente wurden die zwei gängigsten Basen verwendet; Natriumkarbonat und Natriumhydroxid in wässriger Lösung unterschiedlicher Konzentration wurden in die Mikrochips injiziert, die mit den Ölen der OMV (8th TH, 16th TH Lagerstätten) vorgesättigt wurden – diese Proben haben eine hohe TAN (total acid number). Eine weitere Probe der Flysch Lagerstätte, welche eine niedrige TAN aufweist, wurde als Referenz verwendet. Die Injektionsexperimente wurden dazu im sekundären und tertiären Modus durchgeführt.

Die Flysch-Öl Probe zeigte in den Experimenten die höchst Ölgewinnung durch reine Wasserflutung; eine mögliche Erklärung bietet das günstige Mobilitätsverhältnis der

involvierten Fluide. Die Öle mit einer hohen TAN konnten besser mittels alkalischer Lösungen produziert werden. Auch zeigte die Injektion von Natriumkarbonat-Lösungen eine bessere Verdrängungseffizienz als Natriumhydroxid. Dies spricht für eine dominante Rolle der divalenten Ionen in der Interaktion an den Flüssigkeits-Flüssigkeits-Grenzflächen. „Wasser-in-Öl" und „Öl-in-Wasser Emulsionen" konnten abhängig von der Konzentration der Lösung und der Öl Proben beobachtet werden. Größere Öl-Wasser-Grenzflächen und „Öl-Fäden" wurden als Resultat einer reduzierten Oberflächenspannung im Porenraum beobachtet. Die Experimente zeigen ferner, dass ein höherer Gesamtentölungsgrad im sekundären Modus erreicht werden kann im Vergleich zur Wasserflutung mit anschließender tertiären Flutungen.

Table of Contents

List of Figures

List of Tables

Nomenclature

ΔP	Differential pressure	[bar]
μ	Viscosity	[cp], [Pa.s]
σ	Interfacial tension	[dyne/cm]
∇P	Pressure gradient	[bar/cm]
A	Cross sectional area	[cm^2]
d_{sng}	Syringe inner diameter	[mm]
K_{abs}	Absolute permeability	[Darcy]
K_{rw}	Relative permeability to wetting phase	[-]
L	Length	[cm]
l_{cl}	Cluster length	[m]
N_C^{macro}	Macroscopic capillary number	[-]
N_C^{micro}	Microscopic capillary number	[-]
P_c	Capillary pressure	[Pa]
q$_{inj}$	Injection flow rate	[mm^3/h]
q	Flow rate	[cm^3/s]
u_D	Average (Darcy) velocity	[cm/s], [m/s]
v_{int}	Interstitial velocity	[m/s]
v_{pb}	Pusher block velocity	[mm/h]

Abbreviations

CDC	Capillary Desaturation Curve
CMC	Critical Micelle Concentration
DPT	Differential Pressure Transmitter
EOR	Enhanced Oil Recovery
HC	Hydrocarbon
IFT	Interfacial Tension
O/W	Oil in Water
PDMS	Polydimethylsiloxane
PMMA	Polymethylmethacrylate
REA	Representative Elementary Area
RIE	Reactive Ion Etching
TAN	Total Acid Number
TH	Torton Horizon
W/O	Water in Oil

Chapter 1

Introduction

Over the past decades, the global demand for energy has been increasing. As fossil fuels have been a major source of energy, general interest lies in the improvement of hydrocarbon (HC) production technologies. A typical conventional ultimate oil recovery (also called primary and secondary recovery) has an average value of 35% (Lake 2014), which implies that a substantial amount of oil is still left behind and trapped. Tertiary recovery or in other words, enhanced oil recovery (EOR), is a bundle of techniques with the primary focus on increasing the recovery by targeting the unrecovered trapped and/or bypassed oil in the reservoir at the end of conventional production.

Chemical flooding is one of the EOR techniques aiming to release capillary trapped oil. The injection of alkalis, surfactants and a variety of their combination belong to this family of recovery techniques.

Alkaline flooding is probably the cheapest chemical EOR method (Sheng 2013). In this process, a high pH solution is injected into the reservoir and upon contact with the crude oil, it reacts with the saponifiable components. The consequence is an in-situ generation of surface active agents or soaps that results in IFT reduction. Significant amounts of multivalent cations such as calcium and magnesium are present in the formation brine. These ions precipitate as they mix with the alkaline solution causing permeability damage and also reduction in multivalent cation activity in the brine, resulting in more surfactant activity and lower IFT values (Mayer et al. 1983). The alkaline solution also reacts with the reservoir rock as it flows through the reservoir. Hydrogen ions present on the surface of clay minerals consume the alkaline solution hydroxide ions and consequently, the pH of the solution decreases. Other than the precipitation due to the alkaline – brine reactions, if the reservoir rock also contains divalent ions such as calcium and magnesium, further precipitation may occur and essentially may lead to pore

plugging. Therefore, in order to have a successful chemical flood, pore level understanding of fluid-fluid and rock-fluid interactions is crucial.

OMV is contemplating a recovery boost by performing alkaline-polymer flooding in Matzen oil field that have been undergone conventional production over 60 years.

Microfluidic devices – artificial porous media – have proved to be a robust tool for studying pore level behavior of fluid-fluid interactions (Karadimitriou, Hassanizadeh 2012). In this work, microfluidic chips were utilized to investigate the effects of alkaline flooding on oil recovery and to study pore scale fluid-fluid interactions. The influence of parameters such as alkaline types, concentrations and total acid number (TAN) were studied in detail. In the alkaline flooding experiments, which were performed as secondary and tertiary oil recovery methods, oil samples from Matzen (16th TH and 8th TH reservoirs) and St. Ulrich (Flysch reservoir) oil fields were utilized.

1.1   Background and Context

Many oil reservoirs located in Austria have been flooded with water for years. It is safe to assume that a large amount of oil is bypassed and cannot be produced by conventional waterflooding anymore. Therefore, EOR methods are required to improve the recovery. Alkaline flooding is believed to be a cheap and efficient approach for enhancing the recovery of heavy oils. OMV is comprehensively studying the effects of alkaline flooding methods on Austrian reservoirs containing heavy oil with high TAN.

In this thesis, oil samples provided by OMV were used to conduct several alkaline flood experiments using microfluidic devices. In order to contrast the results and reach an accurate conclusion, a low TAN oil sample from Flysch reservoir was provided and utilized likewise, in assistance to inspect the importance of TAN in alkaline injection experiments. As a deduction, pore-level observations and interactions were recorded and studied for the available high and low TAN oil samples.

1.2   Scope and Objectives

The aim of this thesis is to establish a workflow for laboratory flooding and microfluidic experiments to examine alkaline flooding in real time and to provide the first steps in image and data analysis.

First, the available equipment was inspected followed up by the execution of different microchip cleaning procedures, which contributed as a base for the proposed cleaning procedure.

Next, alkaline flooding experiments were conducted to investigate the effects of alkaline type and concentration on the three available oil samples under secondary and tertiary recovery methods. Alkaline solutions were prepared by the utilization of the two most common alkaline salts: sodium carbonate and sodium hydroxide.

Finally, the experimental results were submitted for image preparation and analysis performed using ImageJ software. An image processing workflow and a procedure automation were proposed after systematically testing several image analysis techniques.

1.3 Overview

Chapter 1 motivates and outlines the thesis.

In chapter 2, a brief introduction to enhanced oil recovery methods, alkaline flooding procedures and mechanisms is presented.

Chapter 3 gives an overview of the laboratory equipment. Microfluidic devices and their manufacturing methods are described and in addition, available pumps are evaluated with respect to stability of flow rate and a comparison has been performed.

Chapter 4 provides the applied experimental design and instructions to characterize the microfluidic chips. Porosity and permeability of different available microchips are evaluated and presented followed up by a detailed description of the tested and proposed cleaning and preparation procedures. Moreover, the image analysis process and automation procedure are discussed briefly. Finally, the properties of the provided oil samples and the designed experimental scenarios are introduced.

In chapter 5, calculated oil recoveries for the different flooding scenarios are given and microscope taken images are analyzed. Some images and notable observations are shown and further discussed. In addition, oil saturation changes and oil recoveries versus time are plotted and presented.

Chapter 6 summarizes and concludes the thesis.

Chapter 2

State of the Art

This chapter gives a brief overview of enhanced oil recovery, alkaline flooding and its related recovery mechanisms.

2.1 Enhanced Oil Recovery

Generally, hydrocarbon (HC) recovery is classified into three leading stages:

- Primary recovery: natural forces present in the reservoir are utilized as the main driving mechanism.
- Secondary recovery: gas or – most commonly – water is injected into the reservoir under immiscible conditions. The goal is (a) pressure maintenance and (b) viscous displacement of hydrocarbons.
- Enhanced oil recovery (EOR): any approach implemented after secondary recovery; however, in some cases such as heavy oil reservoirs, primary and secondary recovery stages might be skipped.

Primary and secondary recoveries that are commonly termed as conventional recovery, have a typical average recovery of 35% (Lake 2014), which implies that a substantial amount of hydrocarbon is still left behind in the pore system by the end of secondary stage. The remaining oil is generally trapped in the form of isolated droplets or ganglia caused by capillary forces. At this stage, the magnitude of capillary forces – holding the oil in place – is comparably higher than the viscous forces applied by the waterflood. In other words, further recovery of trapped oil is not possible by means of conventional floods and is the goal in the majority of EOR methods.

EOR refers to oil recovery by injection of materials not normally present in petroleum reservoirs (Lake 2014). These processes are typically subdivided into five main categories:

mobility control, chemical (surfactant), miscible (solvent), thermal and other processes such as microbial methods (Green, Willhite 1998).

Chemical flooding is one of the EOR techniques that encompasses the injection of alkalis, surfactants and a variety of their combinations. Chemical (surfactant) flooding is any process that uses a surface active agent (a surfactant) to bring about improved oil recovery (Lake 2014). In other words, reducing capillary forces is the primary means of oil recovery in chemical flooding. Surfactants may be either injected or generated in-situ by injecting alkaline solutions.

2.2   Chemical EOR

Additional non-wetting phase (e.g. oil) mobilization in porous media can be predicted by the balance of viscous forces and capillary forces, which is called capillary number.

One of the simplest and most widely used definition of capillary number referred to as microscopic capillary number is as follows:

$$N_C^{micro} = \frac{v_{int}\mu}{\sigma} \tag{2.1}$$

Where N_C is the capillary number, v_{int} is the interstitial velocity, μ is the viscosity of displacing fluid and σ is the IFT.

Residual oil saturation relationship with dimensionless microscopic capillary number had been proved by experiments (Moore, Slobod 1956; Abrams 1975) and is shown via capillary desaturation curves (CDCs). Figure 2-1 shows a schematic CDC.
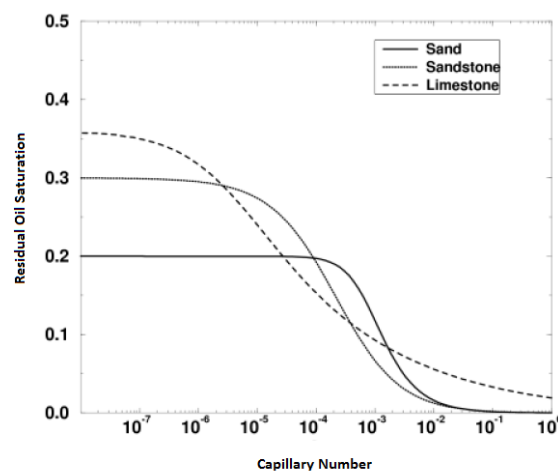
Figure 2-1 – Schematic capillary desaturation curves for sand, sandstone and limestone.

Further experimental data showed that the mobilization of the residual trapped non-wetting phase occurs at N_C^{micro} between $10^{-5} – 10^{-7}$ (e.g. Dullien 1979). These results, however, are

limited to the tested rock type and thus, are non-predictive. Moreover, mobilization is expected to occur at a ratio of viscous to capillary forces of 1. The inconsistency arises from the definition of N_C^{micro} in equation (2.1), which is actually an interfacial definition balancing the viscous stress at a liquid-liquid interface to the interfacial stress at the same interface (Leal 2007). In other words, the definition of N_C^{micro} assumes that viscous and capillary forces act over the same length scale and omits the configuration of the trapped non-wetting phase topology (Armstrong et al. 2014).

For the first time, Melrose and Brandner (1974) defined a criterion that accounts for the non-wetting phase and pore-space topology and introduced the term, macroscopic capillary number. Modifications were done by Hilfer and Øren (1996) after a detailed scaling analysis by connecting the micro- and macroscopic pictures. However, non-wetting phase desaturation was still observed at macroscopic capillary number below 1 (Armstrong et al. 2014). Armstrong et al. (2014) proposed and validated a slightly modified version of the macro-scale capillary number presented by Hilfer and Øren (1996) by including relative permeability into the equation as follows:

$$N_C^{macro} = \frac{l_{cl}\mu u_D}{k_{rw}P_c} \tag{2.2}$$

Where N_C^{macro} is the capillary number, l_{cl} is the cluster length, μ_w is the viscosity of displacing fluid, u_D is the Darcy velocity, k_{rw} is the relative permeability to displacing fluid and P_c is the capillary pressure.

In chemical EOR methods, surface active agents or surfactants are utilized to reduce the capillary forces by lowering the interfacial tension (IFT)[1]. By introducing surfactants into the system, the IFT between two immiscible fluids, the displacing and the displaced fluids, can be reduced. As a consequence, capillary pressure decreases and trapped isolated oil droplets can be remobilized and displaced. Oil ganglia become connected ahead of the displacing fluid front and form an oil bank (Green, Willhite 1998). As the process proceeds, the oil bank grows in

---

[1] IFT term is used when two coexisting immiscible fluids are liquids and surface tension is commonly used when one of the phases is gas.

saturation and volume yielding to a higher oil mobility due to a relative permeability effect. Figure 2-2 shows a scheme of oil bank formation ahead of the EOR injected slug.
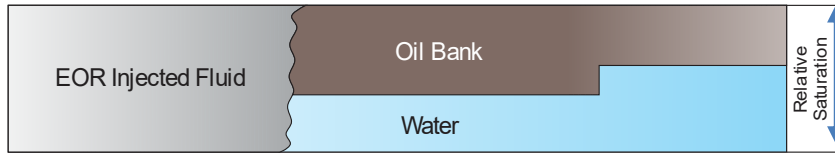
Figure 2-2 – Oil bank formation in chemical EOR flood.

Surfactants can be either directly injected into the reservoir or generated in-situ by the injection of an alkaline solution. Alkaline flooding (also known as caustic flooding) is probably the cheapest chemical method (Sheng 2013) and is therefore attractive and under intensive investigation for flooding reservoirs containing high amounts of saponifiable components. Alkaline flooding is the focus of this work and will be discussed comprehensively in the next section.

2.3   Alkaline Flooding

As previously mentioned, the aim of alkaline flooding is to generate surfactants in-situ, which are called soaps (in order to differentiate from the injected species). In this process, a high pH aqueous solution, which is achieved by the dissociation of alkalis, is injected into the reservoir. Several types of alkaline salts can be applied for in-situ generation of soaps. However, frequently used ones in EOR applications are sodium hydroxide, sodium carbonate and sodium orthosilicate. Dissociation of an alkali yields an increase in hydroxide ion concentration in the solvent and consequently results in a high pH environment. For example, dissociation of sodium hydroxide is as follows:

$$NaOH \rightarrow Na^+ + OH^- \tag{2.3}$$

Sodium carbonate dissociates as:

$$Na_2CO_3 \rightarrow 2Na + CO_3^{2-} \tag{2.4}$$

Followed by hydrolysis process:

$$CO_3^{2-} + H_2O \rightarrow HCO_3^- + OH^- \tag{2.5}$$
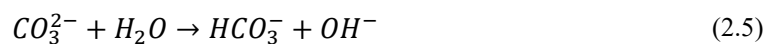
The increase of hydroxide ion concentration leads to a decrease in hydrogen ion concentration, or pH in better words, that is described as:

$$pH = -\log[H^+] \tag{2.6}$$

Where $[H^+]$ is the molar concentration of hydrogen ion. Figure 2-3 shows attained pH versus concentration for a variety of alkalis. As illustrated, by using sodium hydroxide (line no. 1) very high pH can be achieved, which triggers more alkaline consumption and secondary reactions that gives rise to emulsion and scaling problems (Sheng 2011). Therefore, the general interest in applying sodium hydroxide reduced.

It is worth mentioning that pH of a solution can be affected by its salinity. Solutions of equal alkalinity but different salt content could have different pH values. The effect of salinity on the pH of the solution varies for different alkalis. For example it has been observed that the pH of sodium carbonate solution is less dependent on salinity (Labrid 1991).
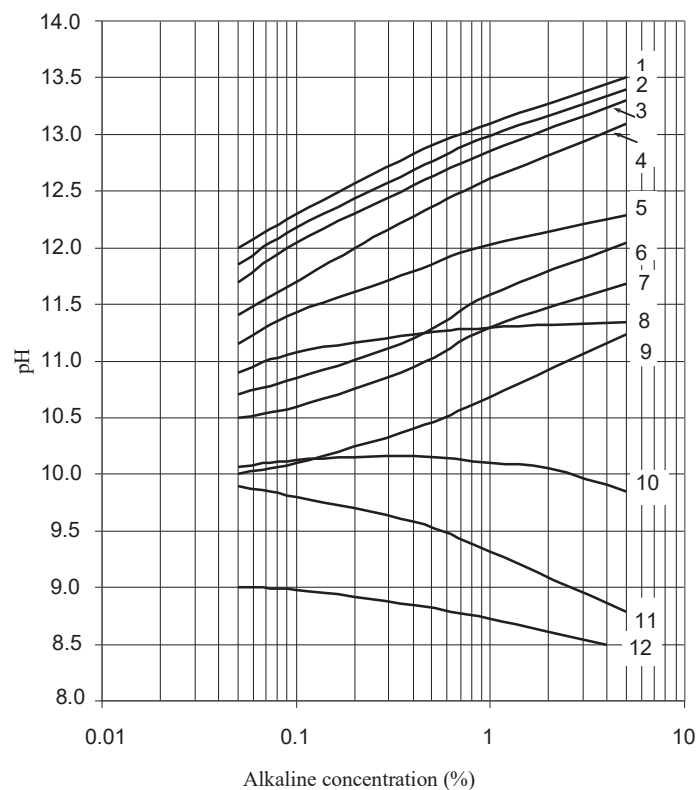
Figure 2-3 – Graph of pH values of alkaline solutions at different concentrations at 25°C: 1, sodium hydroxide [NaOH]; 2, sodium orthosilicate [Na$_4$SiO$_4$]; 3, sodium metasilicate (water glass or liquid glass, [Na$_2$SiO$_3$]); 4, sodium silicate pentahydrate [Na$_2$SiO$_3$·5H$_2$O]; 5, sodium phosphate [Na$_3$PO$_4$·12H$_2$]; 6, sodium silicate [(Na$_2$O)(SiO$_2$)$_n$, n = 2, where n is the weight ratio of SiO$_2$ to Na$_2$O.]; 7, sodium silicate [(Na$_2$O)(SiO$_2$)$_n$, n = 2.4]; 8, sodium carbonate [Na$_2$CO$_3$]; 9, sodium silicate [(Na$_2$O)(SiO$_2$)$_n$, n = 3.22]; 10, sodium pyrophosphate [Na$_4$P$_2$O$_7$]; 11, sodium tripolyphosphate [Na$_5$P$_3$O$_{10}$]; and 12, sodium bicarbonate [NaHCO$_3$] (Sheng 2011).

Significant amounts of calcium and magnesium cations are present both in reservoir brines and on the rock surfaces. Once the alkaline solution contacts either the brine or the rock,

precipitation of calcium and magnesium occurs in the form of hydroxides, carbonates or silicates depending on types of alkali used. Figure 2-4 shows alkali precipitation extent and resulting permeability damage in the presence of hard water under equivalent experimental conditions of porosity and flow rate. As can be seen on the plot, the degree of permeability damage is much higher for precipitation of silicates compared to that of carbonates. This attributes to the high plugging nature of silicate precipitates since they are typically hydrated and flocculent. In contrary, carbonate precipitates are relatively granular and less adhering on solid surfaces (Cheng 1986). Furthermore, carbonate precipitates can be removed successfully by acidizing or by using inhibitors whereas no long-term treatment exists for removing silicate precipitates.
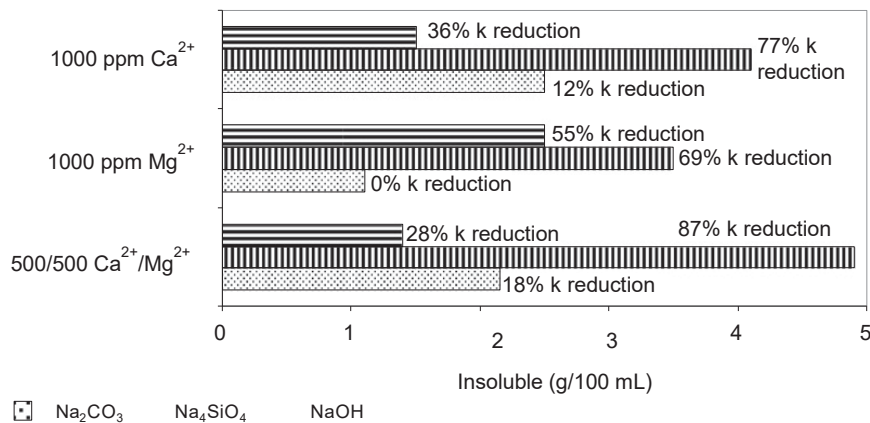
Figure 2-4 – Extent of alkali precipitations (represented by %) and permeability damage (represented by the lengths of bars) for different hardness solutions (Sheng 2011; Cheng 1986). Contrary to silicates, carbonate precipitates have a rounded shape and less adhering tendency to solid rocks, hence the corresponding permeability damage is lower than that of silicates.

In terms of IFT reduction, it has been observed that all commonly used alkalis have comparable effectiveness (Campell 1982; Burk 1987).

Dissociation of alkalis causes an increase in alkalinity and in salinity. Alkali concentration (pH) and salinity (ionic strength) have different effects on IFT. It has been observed that the range of alkali concentration in which the IFT between acrude oil and alkaline solution is at the minimum is very narrow (Sheng 2011). Figure 2-5 shows the dynamic IFT between a crude oil and sodium hydroxide solution with different concentrations at a fixed salinity of 0.01 mol/L. In this figure, NaOH solution with a concentration of 0.0001 mol/L (curve 1) exhibits almost no IFT change, as the NaOH concentration is not enough to generate adequate amount of soap at the oil-water interface. Using a solution with 0.0005 mol/L NaOH (curves 2) results in a short lasting IFT reduction. The IFT increases again as the soap molecules leave the interface

and enters the aqueous phase. An optimum concentration of NaOH (for the given salinity) is observed at 0.001 and 0.005 mol/L (Curves 3 and 4) at which a relatively stable reduced IFT is achieved. Higher concentrations of NaOH (0.01 mol/L, curve 5) yields a temporary reduction in IFT as the soap is generated at the interface. The temporary reduction of IFT at high concentration of NaOH is attributed to dominant effects of salinity over the alkalinity impacts (Zhao et al. 2002).
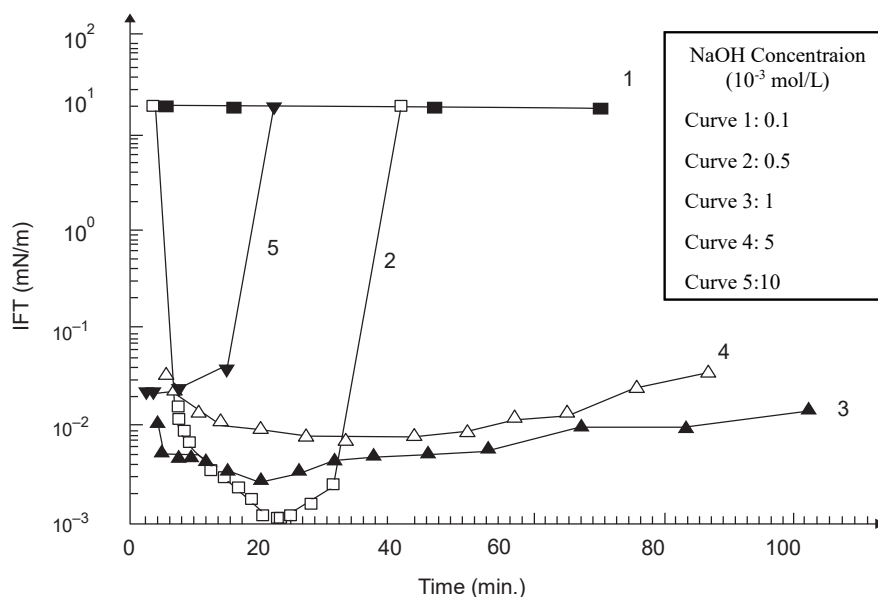
Figure 2-5 – Dynamic IFT between crude oil and NaOH solution with [Na$^+$] of 0.01 mol/L at 30°C (Sheng 2011; Zhao et al. 2002).

2.3.1 Alkaline – Crude Oil Interactions

Soaps are generally the alkali salt (mostly sodium and potassium) of fatty acids. Fatty acids, in simple words, are carboxylic acids (-COOH) with a long hydrocarbon chain (typically denoted by R). A soap molecule, as shown in Figure 2-6 has a polar head, which is hydrophilic and a non-polar tail that is hydrophobic. Aggregation of these molecules at the interface of two immiscible phases, namely water and oil, will reduce the interfacial tension.

Reaction of alkaline solution with oils that have sufficient amounts of saponifiable (also called acidic) components, results in soap generation. The main fraction of saponifiable components is comprised of fatty acids that is denoted by RCOOH. When they react with a high pH solution, RCOO$^-$, which is a bundle of water soluble anionic, surfactants are generated. The following equation shows the reaction of sodium hydroxide with fatty acids.

$$RCOOH + NaOH \leftrightarrow RCOO^- + Na^+ + H_2O \tag{2.7}$$
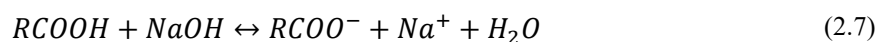
In this context, all saponifiable components are presented as a single active acid component denoted by HA. Acid number is a measure to quantify the amount of acid components in the oil and is defined as the milligrams of potassium hydroxide required to neutralize one gram of oil. It is worth mentioning that not all the oil acidic components are surface active, hence a high acid number is not a sufficient recovery criterion (deZabala et al. 1982).
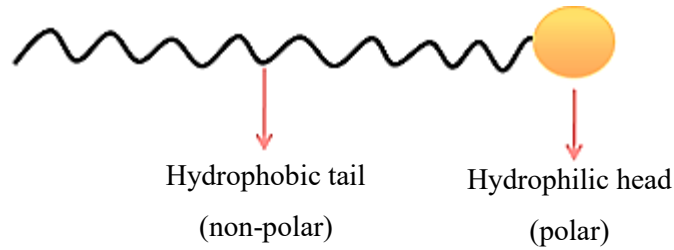
Figure 2-6 – General representation of a soap molecule (amrita.olabs.edu.in 2013).

The acid component in crude is sufficiently insoluble in the aqueous phase at neutral pH that copious waterflooding will not extract it (deZabala et al. 1982). By introducing high pH aqueous media, oil soluble acid component partitions into aqueous phase according to partitioning coefficient:

$$HA_o \leftrightarrow HA_w \tag{2.8}$$

$$K_D = \frac{[HA_w]}{[HA_o]} \tag{2.9}$$

Where K_D is the partitioning coefficient and subscripts o and w denote oleic and aqueous phases, respectively. Acid component dissociates in aqueous phase as:

$$HA_w \leftrightarrow H^+ + A^- \tag{2.10}$$

H^+ is consumed by OH^- present in the high pH aqueous medium and the concentration of A^-, which is a soluble anionic surfactant, increases:

$$H^+ + A^- + OH^- \leftrightarrow H_2O + A^- \tag{2.11}$$

By consumption of H^+, the concentration of HA_w decreases, and equilibrium (2.8) shifts to the right. Figure 2-7 illustrates a schematic of alkaline recovery process.
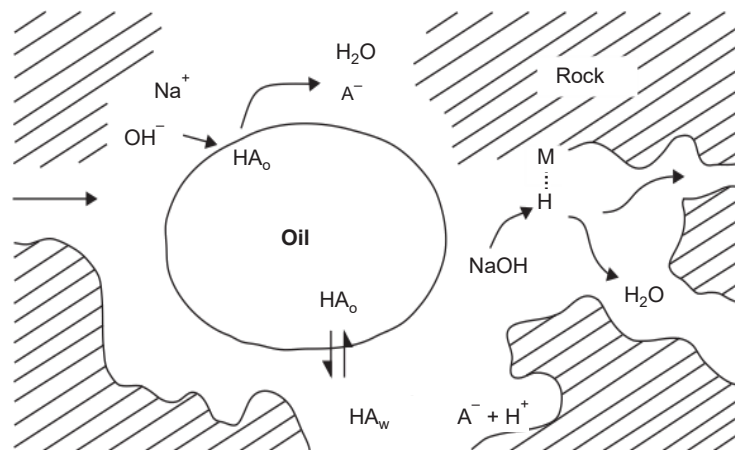
Figure 2-7 – Schematic of alkaline recovery process (deZabala et al. 1982).

In addition to a decreasing capillary pressure, emulsification is another outcome of lowered IFT. Once the total concentration of soap (surfactant) molecules surpasses the critical micelle concentration (CMC), monomers will aggregate and form micelles. Micelles have no contribution in reducing IFT, therefore, above CMC, no further IFT decrease happens. Figure 2-8 demonstrates a schematic of micelle formation and the CMC (Mukerjee, Mysels 1971; Biolin Scientific). Under certain conditions, micelles can form water-in-oil (W/O) and/or oil-in-water (O/W) microemulsions. Microemulsions are translucent, thermodynamically stable, isotropic liquid mixtures of oil, water and surfactant (Sheng 2011), which play a key role in chemical EOR processes.

2.3.2 Alkaline – Brine Interactions

Reservoir brines contain significant concentrations of ions such as calcium and magnesium. Once alkaline solution contacts the reservoir brine, precipitation of these cations in the form of calcium or magnesium hydroxide, carbonate and silicate occurs depending on the used alkali salt. This process reduces the activity of multivalent cations present in the reservoir brine and causes permeability damage. On the other hand, the reduction in brine salinity gives rise to more surfactant activity, resulting in lower IFT values (Mayer et al. 1983).

Silicates have shown more IFT reduction in hard water compositions that can be attributed to high pH and very low solubility of their precipitates rather than that of hydroxides and carbonates (Novosad, et al. 1981). Nevertheless, their contribution in damaging permeability must not be underestimated.
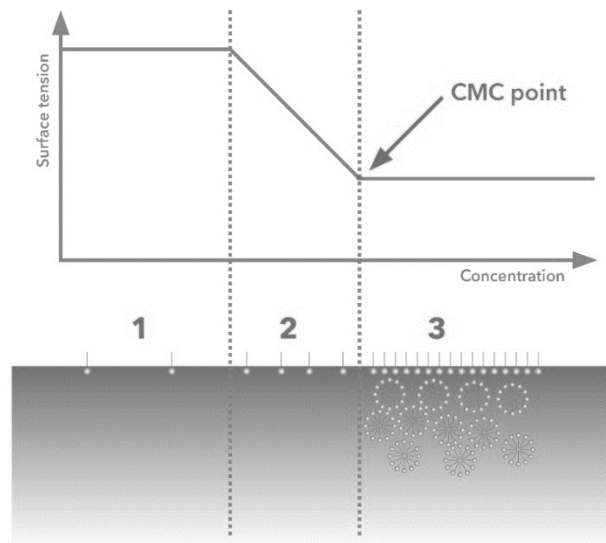
Figure 2-8 – A schematic illustration of CMC and surface tension vs surfactant concentration. At region 1, the concentration of soap monomers are not enough to lower IFT. Region 2 shows IFT decrease as the monomers concentration is increasing at the interface. Region 3 starts as the CMC is reached and IFT shows no further reduction. (Mukerjee, Mysels 1971; Biolin Scientific).

2.3.3 Alkaline – Rock Interactions

Reservoir rocks have typically complex mineralogy and alkali can react with many commonly found minerals in reservoir rocks (Lake 2014). Therefore, quantifying the alkaline-rock interaction is quite complicated and not yet well established. Alkaline reactions with rock can be divided into two main categories, which yields to a decrease in pH of the solution and in alkaline consumption (Sheng 2011):

- Alkaline – rock ion exchange
- Alkaline – rock direct reaction

Alkaline – rock ion exchange is a fast and reversible process in which ions are exchanged between the rock surface and alkaline solution. Clay minerals have a flat sheet-like structure. In other words, they have a high surface area that makes their role very important in alkaline-rock ion exchange processes. Once alkaline system contacts the rock, ions such as hydrogen, magnesium and calcium, which are present in clays, will exchange for alkali ions in solution, namely Na^+. Equation (2.12) describes the alkaline-rock hydrogen exchange process whereas equations (2.13) and (2.14) show divalent cation exchange reactions.

$$H \cdots M + Na^+ + OH^- \leftrightarrow Na \cdots M + H_2O \qquad (2.12)$$

$$Ca \cdots M_2 + 2Na^+ + 2OH^- \leftrightarrow 2(Na \cdots M) + Ca(OH)_2 \qquad (2.13)$$

$$Ca \cdots M_2 + 2Na^+ + CO_3^{2-} \leftrightarrow 2(Na \cdots M) + CaCO_3 \qquad (2.14)$$
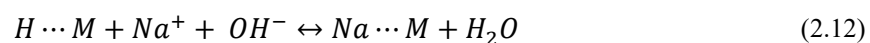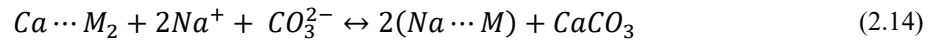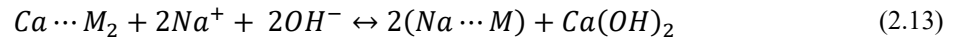
In the above reactions, M denotes mineral-base exchange sites (Figure 2-7). Equation (2.12) shows the exchange of hydrogen ions present on the surface of rock (M) with alkali ions (Na^+). Then hydrogen ions react with hydroxide ions present in the solution and form water (Bunge, Radke 1982). Consequently, the pH of the solution decreases.

Equations (2.13) and (2.14) show the consumption of alkali due to ion exchange with divalent cations (Ca^{2+}) present on the rock surface. As the calcium enters the solution, it reacts with anions present in the solution and forms calcium hydroxide and carbonate precipitates, which leads to pH decrease.

Commonly, a sodium carbonate buffer is used to fill the active exchange sites and prevent the base consumption by ion exchanges.

Alkaline – rock direct reaction is a long-term irreversible process (Sheng 2011) in which incongruent dissolution[2] of specific rock minerals such as fine silica and clay minerals occurs and precipitates appear. Pore plugging may happen as a result of these reactions.

Equations (2.15) and (2.16) describe the dissolution of anhydrite and silica (Stumm, Morgan 1970), respectively. Calcium hydroxide is a less soluble mineral rather than anhydrite.

$$CaSO_{4(s)} + 2NaOH \rightarrow Ca(OH)_{2(s)} + Na_2SO_4 \qquad (2.15)$$

$$SiO_2 + 2H_2O \rightarrow Si(OH)_4 \qquad (2.16)$$

---
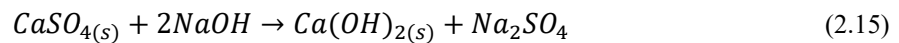
[2] Incongruent dissolution refers to the dissolution of one mineral and the formation of a second, different mineral (Sheng 2011).

Figure 2-9 shows species of solution silica as a function of pH at 25°C (Bunge, Radke 1982).
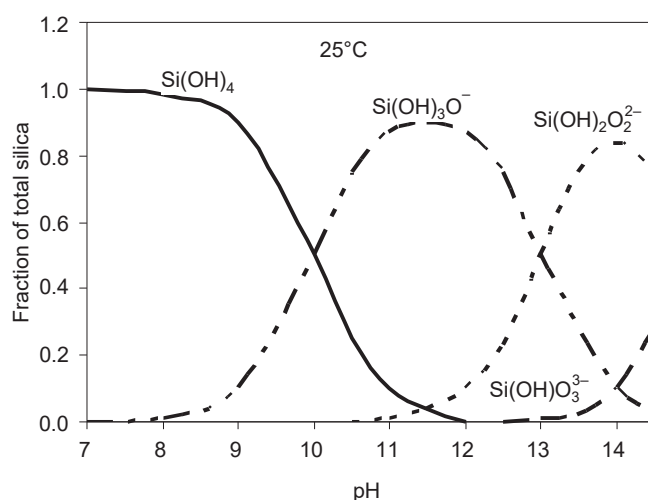
Figure 2-9 – Species of solution silica as a function of pH at 25°C (Bunge, Radke 1982).

The use of carbonate alkalis diminishes carbonate ion release from the rock into the solution. On the other hand, dissolution of minerals is a function of pH and can be lowered by using carbonate alkalis that are weaker than hydroxide or silicate species. Furthermore, the pH of carbonate solutions, namely sodium carbonate, is less dependent on salinity (Labrid 1991).

2.4 Alkaline Flooding Recovery Mechanisms

Several different alkaline flooding recovery mechanisms were summarized by Johnson (1976). This section presents an overview of the three most important ones.

2.4.1 IFT Reduction

As previously mentioned, formation of soaps and their aggregates at oil-water interface may lower the IFT (Ramakrishnan, Wasan 1983). This reduction results in lower capillary forces that are considered the trapping forces. Extend of reduction in IFT is affected by pH (alkali concentration) and salinity (ionic strength) as presented in Figure 2-10.

2.4.2 Emulsification

Emulsion formation can be considered as a consequence of IFT reduction. Additional oil recovery upon emulsion formation can be explained in at least three ways:

Emulsification and entrainment: due to IFT reduction, residual oil emulsifies in water and flows with the aqueous phase. This process improves the displacement efficiency. The conditions for this mechanism are high pH, low salinity and low acid number (Subkow 1942).

Emulsification and entrapment: if the oil in water emulsion size is larger than the pore throat sizes, it will plug the flowing path and leads the fluid to flow through unswept pores. This process enhances the sweep efficiency. High pH, moderate acid number and low salinity are the reported required conditions for the occurrence of this mechanism (Jennings et al. 1974).

Emulsification and coalescence: in this process, water in oil unstable emulsions are ruptured as they contact each other, which results in a continuous oil bank formation. Therefore, an improvement in relative permeability leads to the mobilization of oil. Moreover, some emulsion droplets may block the small pore throats and impose a sweep efficiency improvement. It was observed that alkaline flooding of acidic oils with hydroxides of certain divalent cations increased the oil recovery compared to flooding with hydroxides of monovalent cations. This might be attributed to the promotion of W/O emulsions due to presence of divalent ions (Castor et al. 1981b).
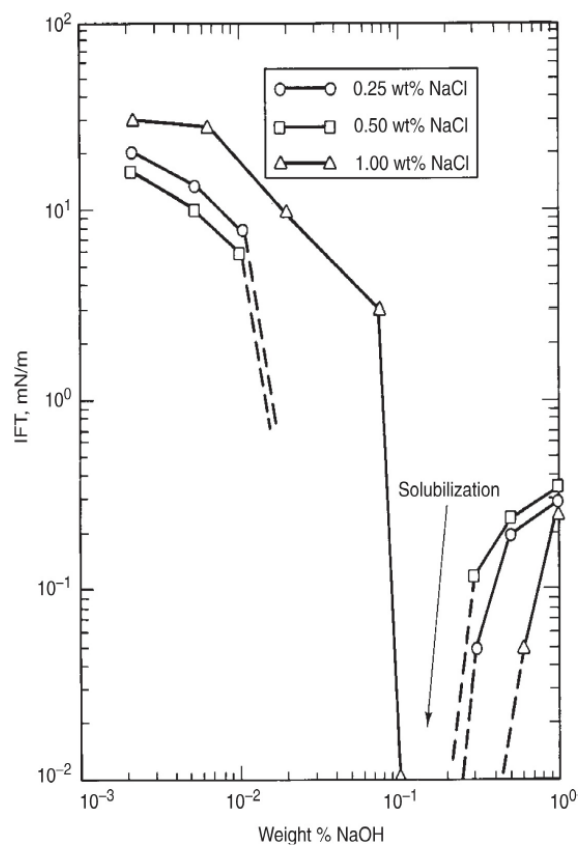
Figure 2-10 – pH and salinity effects on IFT reduction (Ramakrishnan, Wasan 1983).

2.4.3 Wettability Reversal

High pH solution floods may change the wettability as well. This change can be from water- to oil wet or vice versa. Improvement in recovery for each case is explained as follows.

Oil wet to water wet reversal: improvement in oil production is expected when the wettability is changed from oil wet to water wet. This owes to the favourable changes in relative permeabilities.

It has been observed that alkaline floods lowered the water relative permeability (Mungan 1966a) and higher oil recoveries were achieved by wettability reversal mechanism (Mungan 1966b).

Several researchers reported that cores became more water wet after contacted by alkaline solutions and relative permeability curves were shifted to the right (Sheng 2011).

Water wet to oil wet reversal: during this process, a discontinuous non-wetting phase (i.e. residual oil) becomes continuous providing a path for oil to flow. In addition, water drops emulsified in oil tend to block this path. By the blockage of flow, viscous forces increase due to induced high-pressure gradient, hence, these forces can overcome the already reduced capillary forces (Cooke et al. 1974). However, this mechanism needs further discussion.

<div align="right">

Chapter 3

</div>

Experimental Apparatus

This chapter introduces the laboratory equipment employed to perform microfluidic experiments. In addition, some issues that have been observed while utilizing the apparatus are documented and discussed concisely.

3.1   Microfluidic Devices

Microfluidic devices, alias miromodels, are artificial representations of porous media made of a transparent material (Karadimitriou, Hassanizadeh 2012), usually with an overall size of a few centimetres. By the aid of micromodels in conjunction with optical magnifying devices (e.g. microscopes), observation of flow and transport in porous media is achievable.

This section gives an overview of most commonly used micromodel materials and manufacturing methods. Furthermore, the strengths and weaknesses of each are discussed.

3.1.1 Microfluidic Materials

Glass and quartz are two widely used materials for fabricating microfluidic devices, particularly when low depth flow networks, namely up to 20 μm are desired. Micromodels made of glass or quartz resist successfully against relatively high pressures (up to 100 bars) and room temperature changes. Moreover, they manifest nearly no tendency to react with commonly used fluids in EOR experiments and their wettability states are well defined. However, very careful handling is always required since they can easily break. In addition, fabrication of glass and quartz microfluidic devices has drawbacks that will be discussed in section 3.1.2.

Soft materials, like polymethylmethacrylate (PMMA) and polydimethylsiloxane (PDMS) are suitable for making inexpensive micromodels fast (Karadimitriou, Hassanizadeh 2012). Microfluidics made of soft materials have advantages such as being cheap, easy to fabricate

and with no requirement for special laboratory conditions. On the other hand, they swell as a result of reacting with commonly used fluids in two phase flow studies and deform under high pressure injection conditions. In addition, PDMS show wettability change over time.

Silicon has all the advantages of glass and quartz material. However, due to being translucent, it can only be implemented to fabricate pore walls and other transparent materials are required to bind the top and bottom of the microchip. Using two different materials gives rise to mixed wettability properties, which might be a drawback in EOR experiments.

3.1.2 Manufacturing Methods

Etching and soft lithography are two widely used manufacturing techniques of micromodels with EOR study purposes. The etching method is commonly applied when hard materials (e.g. glass and quartz) are being used to fabricate the microchips. The procedure begins with providing a *mask* that is a transparent material on which the desired flow pattern is printed. Exposing to ultraviolet (UV) light, the mask is projected on a substrate (glass, quartz or PMMA) which is spin-coated with photoresist. The substrate is etched using either chemicals (wet etching) or electromagnetic radiation[3] (laser or plasma etching). Areas that are covered by photoresist layer will not be affected by etching agent. Finally, to close the network, a thin wafer of the same material will be bonded on the etched slab. Figure 3-1 demonstrates the etching method. Wet etching technique is relatively easy to apply and can reproduce any network pattern (Karadimitriou, Hassanizadeh 2012). However, pore walls and pore bottoms are curved since liquid acids are isotropic etchants. Laser and ion reactive etching methods are highly accurate, anisotropic and can reproduce any network pattern, but being costly, network depth restrictions and specialized infrastructure requirements make the use of these techniques limited. Furthermore, sealing hard material microchips are always prone to the risk of failure,

---

[3] Electromagnetic radiation is supplied from a laser source or a beam of ions in which the uncovered area of substrate is bombarded with a nobble gas plasma. Transfer of momentum will remove atoms from the substrate surface. This method is also known as ion milling or reactive ion etching (RIE).

especially when the pore network features are very small and enough surface for bonding is not provided.
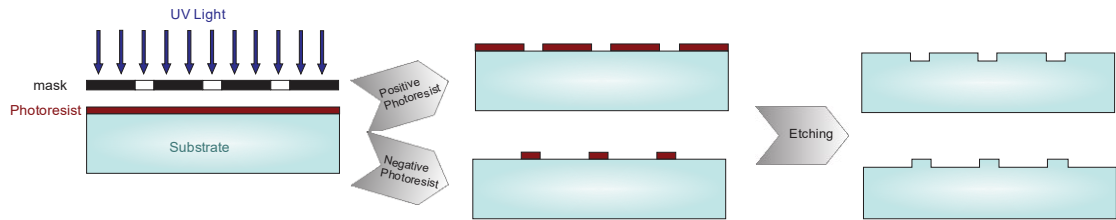
Figure 3-1 – A schematic of micromodel fabrication by etching method.

PDMS is a liquid that is polymerized after mixing with a curing agent (Karadimitriou, Hassanizadeh 2012). Soft lithography is commonly used for fabricating PDMS microfluidics. First, a mask is provided and then projected on a glass or silicon wafer coated with photoresist in the same way explained above. This is called *master wafer*. The master wafer is put in a petri dish followed by pouring a mixture of liquid PDMS and curing agent on it. Then the polymer is degassed and cured. Finally, the PDMS stab is peeled from the master wafer and bonded to a pre-cured thin PDMS slab. Figure 3-2 shows a schematic of PDMS micromodel fabrication. Soft lithography technique is highly accurate, cheap and easy to employ.
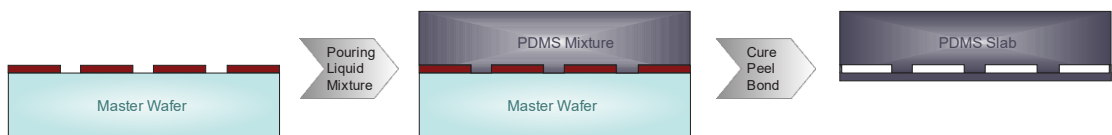
Figure 3-2 – A schematic of PDMS micromodel fabrication.

3.1.3 Microfluidic Chips

EOR microfluidic chips made of borosilicate glass[4], manufactured by Micronit Microtechnologies were utilized for the injection experiments performed in this research. Three different patterns are available:

- Uniform network: channels and pore structures have equal dimensions (Figure 3-3).

- Random network: interconnections and dead-ends with diverse dimensions are distributed randomly (Figure 3-4).

- Physical pore rock network: created based on a limestone sample (Figure 3-5).
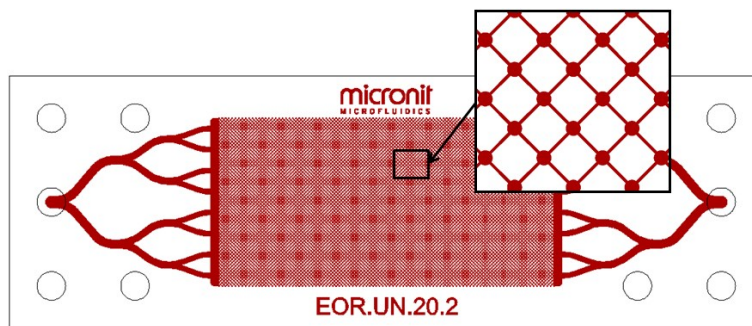
Figure 3-3 – Microfluidic chips with uniform network, porous media is shown in red
(http://www.micronit.com)
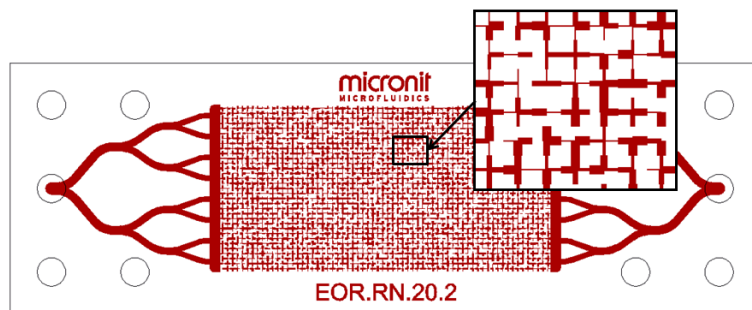
Figure 3-4 – Microfluidic chip with random network, porous media is shown in red
(http://www.micronit.com)

---

[4] Main constituents of borosilicate glass are silica (SiO_2) and boron trioxide (B_2O_3). The low thermal expansion coefficients of such glasses make them resistant to thermal shocks.
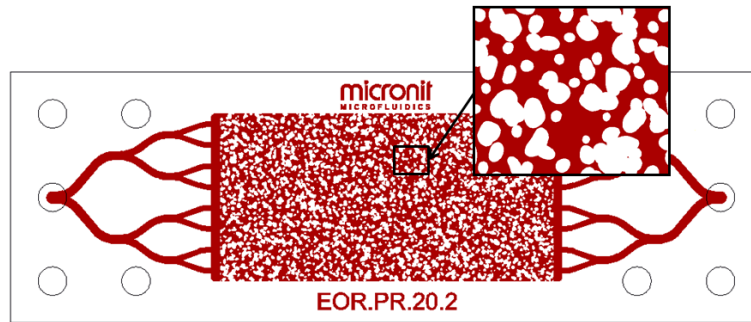
Figure 3-5 – Microfluidic chip with physical pore rock network, porous media is shown in red (http://www.micronit.com)

3.1.4 Chip Holders and Connection Kit

Chip holder and connection kits including Teflon tube, ferrules and tubing to pump connectors were provided by Micronit. As the name implies, it holds the microchip and connects the tubing to the inlet and outlet holes of the micromodels. Two types of chip holders were available:

- Normal chip holder (Figure 3-6), which is made of aluminum. This device can be used at temperatures and pressures up to 80°C and 10 bars, respectively.
- High-pressure chip holder (Figure 3-6) that is made of stainless steel and can withstand operating pressures up to 100 bars.

Figure 3-6 – Normal aluminum (left) and high pressure stainless steel (right) chip holder

The applied tubes were made of Teflon with an inner diameter of 0.25 mm and outer diameter of 1.58 mm. Elastomer ferrules were used to provide a sealed connection between the tubes and microfluidic chips (Figure 3-7).

Figure 3-7 – Teflon tubes and elastomer ferrules

3.2   Visualization System

A Motic AE2000 inverted microscope (Figure 3-8) was utilized to monitor the experiments. With the aid of a mounted digital camera, the microscope was connected to a computer. This made capturing digital images and videos for further analysis possible. However, even with the lowest magnification objective, a full range image of the microfluidic chip was not achievable. Furthermore, due to uneven illumination, obtained images showed a tapered brightness that caused problems in further image analyses. In section 4.3 a methodology for eliminating the adverse effects caused by uneven background light is described.

Figure 3-8 – Motic AE2000 inverted microscope with digital camera

3.3   Injection Equipment

In this thesis, two type of pumps for injection purposes were utilized, a syringe pump and a Vindum pulse free high precision pump. This section gives an introduction to each type briefly.

3.3.1 Syringe Pump

Syringe pumps are cheap and easy to use. They are appropriate for a wide range of experimental and teaching purposes. In syringe pumps, a stepper motor provides an endless screw motion

(screw drive) on which the pusher block is set. The pusher block advances for a given distance at each step of the motor to push the syringe plunger and injecting the fluid. In this thesis, cleaning chemicals were injected using a New Era NE-300 syringe pump (Figure 3-9); however, a high precision Vindum pump was employed to perform the flooding experiments. NE-300 holds a variety of syringes with different inner diameters (from 4.7 to 26.6 mm). It is able to pump a minimum rate of 0.00073 and a maximum rate of 1257 milliliters per hour using syringes with inner diameter of 4.7 and 26.6 mm, respectively. Figure 3-10 shows a plastic syringe and its main components.

Figure 3-9 – NE-300 syringe pump and its major components

To start pumping, the syringe has to be loaded with the fluid of interest, placed on the syringe holder block and locked by the syringe clamp. Then the pusher block has to be aligned with the syringe plunger flange, which is done by pressing and holding the drive nut button. Final step is to set the syringe diameter (in millimeters), which can be either calculated manually or often may be found in manufacturer's catalogues. Inner diameters of used syringes in this research are tabulated in Table 3-1. The pump adjusts the speed of pusher block according to the entered diameter:

$$v_{pb} = \frac{4q_{inj}}{\pi d_{sng}^2} \tag{3.1}$$

Where v_{pb} is the velocity of pusher block, q_{inj} is the desired flow rate and d_{sng} is the inner diameter of syringe.

Table 3-1 – Diameter of available syringes in the reservoir engineering laboratory

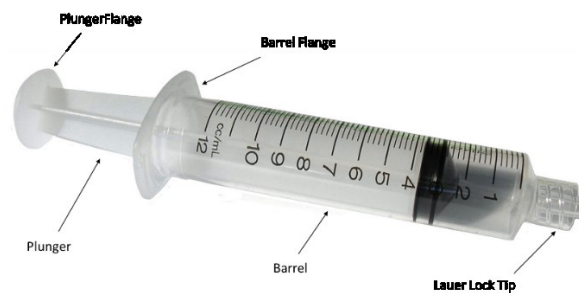| Manufacturer	Material	Volume [ml]	Inner Diameter [mm]
B. Braun	Plastic	3	9.71
	Plastic	10	15.96
Hamilton	Glass	5	10.30
	Glass	10	14.57

Figure 3-10 – Plastic syringe and its main components.

A common problem of syringe pumps is pressure and flow rate oscillations. It is particularly the case when low flow rates are applied (e.g. in microfluidic experiments). At low flow rates, as the pusher block has to move very slowly, the step by step operation of the stepper motor is perceptible leading to the mentioned oscillations. To diminish these pulsations, usage of smaller diameter syringes that results in higher speed of pusher block is recommended. Per contra, this limits the volume of injection fluid. Figure 3-11 indicates the syringe size impact on pulsation. The amplitude of oscillations (pressure instability) is clearly higher when using a 10 ml syringe and the frequency, which is associated with the number of steps, is lower since the block pusher moves slower.

Employing plastic syringes enhances the stability of pressure and flow rate in contrast to those made of glass. The reason is the higher elasticity of plastic compared to glass, which acts as a pressure support in a peristaltic manner.

Another important characteristic when using microfluidic devices is responsiveness. This can be quantified by the elapsed time that the microfluidic system needs to reach steady state flow conditions. The main parameter that affects this elapsed time is the elasticity of microfluidic system, tubes, syringes, etc. It must be noted that using less compressible materials such as glass increases the responsiveness of the system. On the other hand, pulsation is enhanced. As it is evident from Figure 3-12, the pressure instability is higher and responsiveness is lower when glass syringe is used.
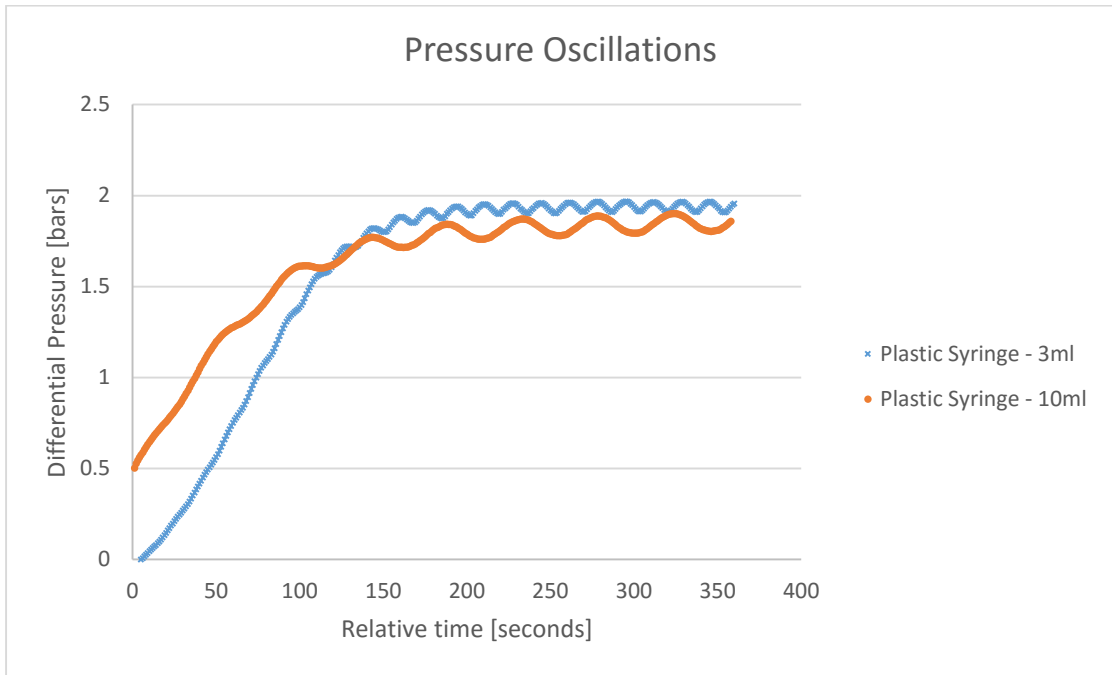
Figure 3-11 – Pulsations recorded for 10 ml and 3 ml plastic syringes. Pressure curve for the 10 ml plastic syringe has an intercept of about 0.5 bar due to a delay in the measurement recording. (q_{inj} =20 ml/h).
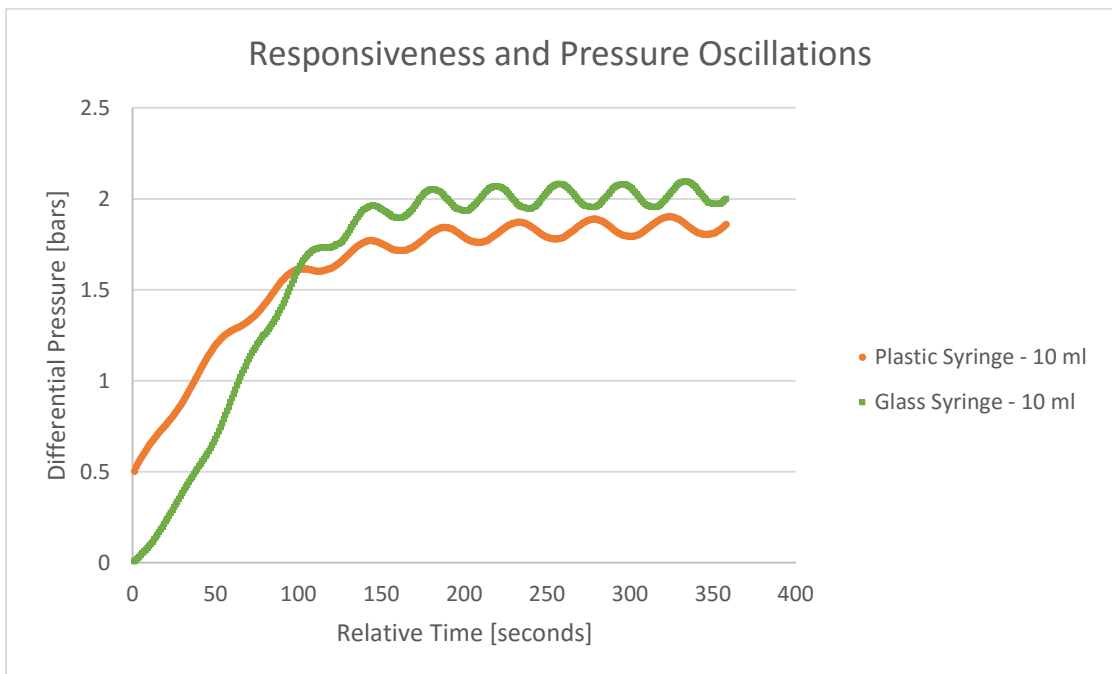
Figure 3-12 – Responsiveness and pulsations recorded for plastic and glass syringes with identical volumes. Pressure curve for the 10 ml plastic syringe has an intercept of about 0.5 bar due to a delay in the measurement recording (q_{inj} = 20 ml/h).

3.3.2 Vindum pulse free high precision pump

A new brand Vindum VP-12K pulse free pump (Figure 3-13) was utilized to conduct water and alkaline solution injection. This gave the opportunity to compare the recorded responsiveness and pulsation curves with the NE-300 syringe pump (Figure 3-14). The available Vindum pump provides a minimum flow rate of 0.0001 ml/min and maximum flow rate of 30 ml/min. Being pulse free and capable to inject continuously from an external reservoir are two of the several advantages of VP-12K. However, it is more expensive and relatively complicated to install and clean if oil or cleaning chemicals are being used.
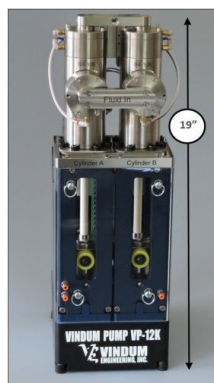
Figure 3-13 – Vindum VP-12K continuous pulse free high-pressure metering pump.
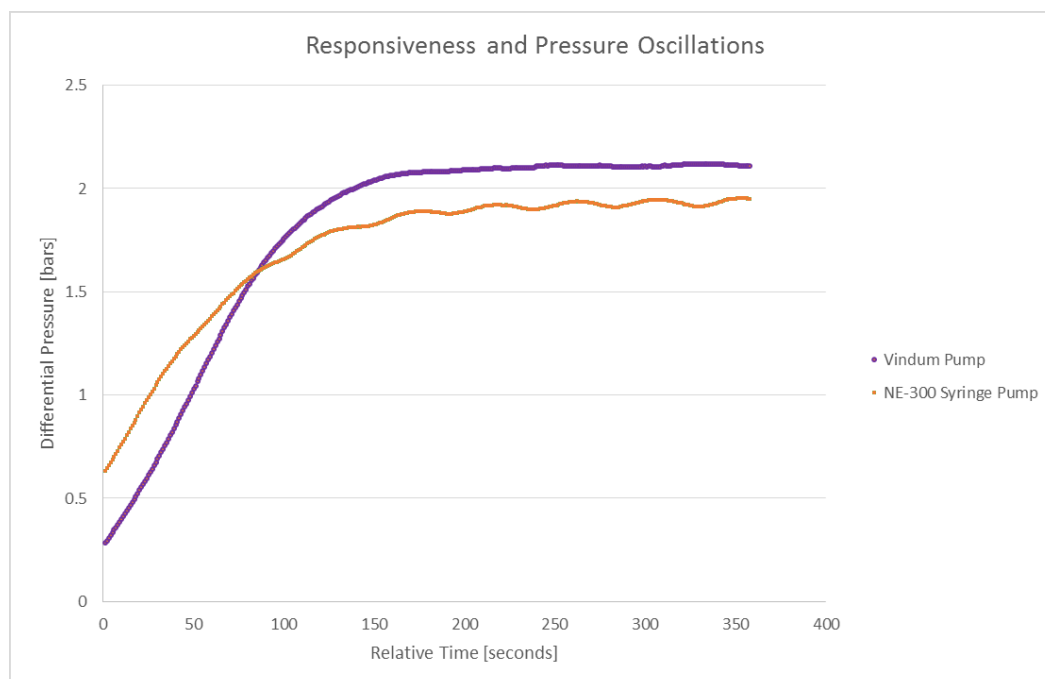
Figure 3-14 – Responsiveness and pulsations recorded for Vindum pump and NE-300 with a 10 ml plastic syringe. Pressure curve for the NE-300 has an intercept of about 0.6 bar due to a delay in the measurement recording (q_{inj} = 20 ml/h).

3.4 Other Equipment

### 3.4.1 Vacuum Pump

The vacuum pump plays an important role when saturating microchips and helps to avoid air bubble trapping. In this thesis, a Welch MPC 301 Z vacuum pump (Figure 3-15 – Welch MPC 301 Z vacuum pumpFigure 3-15) with an ultimate pressure of less than 8 mbar is employed to conduct the experiments. As liquids should not enter the pump, the waste tank was equipped with a sealed lid serving as a liquid trap.

Figure 3-15 – Welch MPC 301 Z vacuum pump

3.4.2 High Precision Balance

Preparation of alkaline solutions and synthetic brine requires a high precision scaling device. A Kern EG series scale with three decimal precision was employed for this purpose (Figure 3-16)

Figure 3-16 – Kern EG 620-3NM high precision balance

3.4.3 Differential Pressure Transmitter

Figure 3-17 shows a Keller PRD 33X differential pressure transmitter that was employed for pressure measurements. This instrument can measure differential pressures range from 0 to 3 bars and line pressures up to 40 bars.

Figure 3-17 – Keller PRD 33X differential pressure transmitter

Chapter 4

Experimental Setup and Methodology

An important step in conducting experimental researches is to design the experiments. The employed equipment setup is schematically displayed in Figure 4-1.
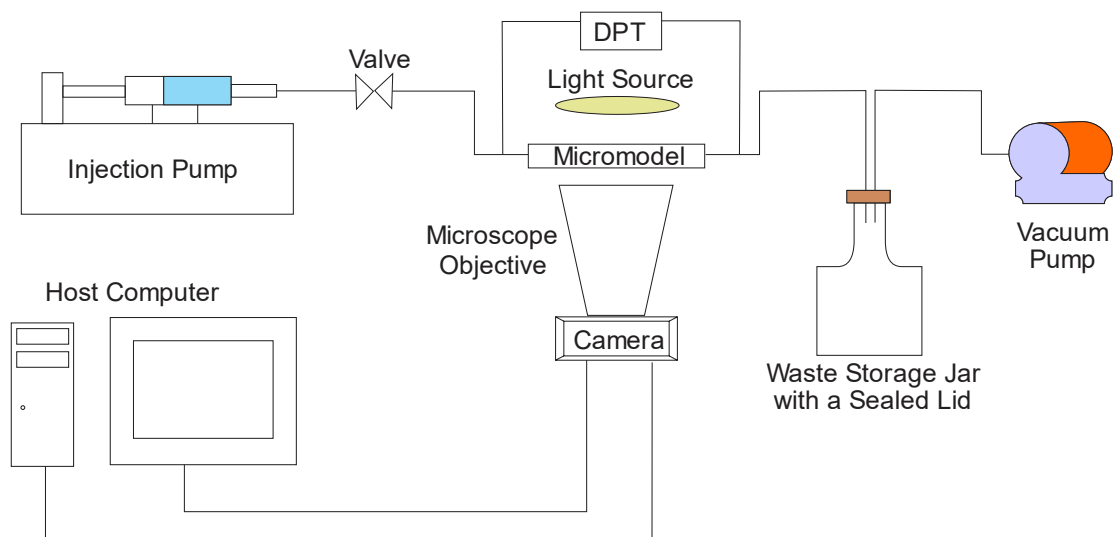
Figure 4-1 – Experimental setup scheme

This chapter presents four important processes, which if not performed correctly, the reliability of results will be indecisive. These procedures are as follows:

- Microfluidic chip characterization
- Microfluidic chip cleaning procedure
- Photo capturing and full range image preparation
- Image analysis

4.1   Microfluidic Chip Characterization

As a starting point for further investigations, porosity and permeability of microchips had to be measured. To do so, the binary drawing files of the three available pore networks provided by Micronit, were processed in "Corel draw®" and "Rhinoceros®". This is required since the received raw drawings are not suitable to perform further analyses.

4.1.1   Porosity Calculation

Porous network lengths, width and area of grains were measured using "Rhinoceros®" (Figure 4-2). Subtracting the total grain area from the bulk area (i.e. product of length and width) defines the areal porosity of the porous medium. Table 4-1 shows the dimensions and calculated areal porosity of the three available microfluidic chips.

Table 4-1 – Measured dimensions and calculated areal properties for three available network types.

Network Type	Porous Medium Length [mm]	Porous Medium Width [mm]	Bulk Area [mm^2]	Total Grains Area [mm^2]	Pore Area [mm^2]	Areal Porosity [%]
Uniform	19.961	10.090	201.406	80.959	120.447	59.8
Random	19.760	10.040	198.390	111.394	86.996	43.8
Physical Rock	19.960	10.040	200.398	75.397	125.001	62.4

It is worth mentioning that all the applied microfluidic chips were manufactured by wet etching method. As previously mentioned (section 3.1.2), liquid acid erodes the glass in an isotropic way, therefore pore walls will not be vertical. Figure 4-3 shows the documented design rules provided by Micronit. Curved walls imply a difference between areal and volumetric porosity and fluid saturations. However, acceptable experimental results are achievable using merely areal properties. Table 4-2 presents the calculated volumetric porosity based on the pore volume reported by the manufacturer.
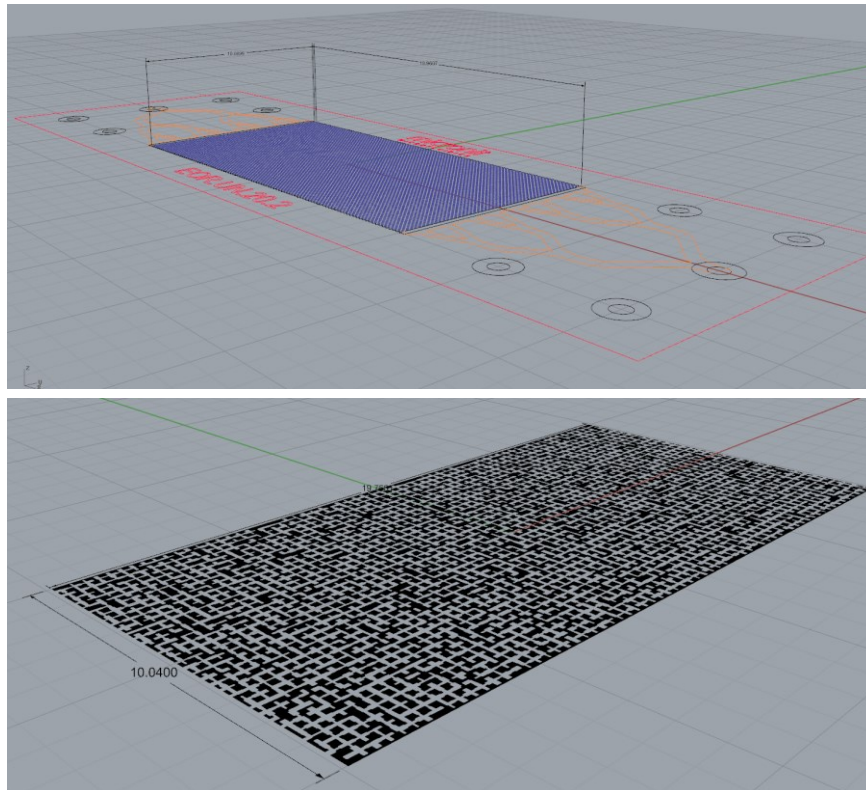
Figure 4-2 – Dimension measurements and porosity calculation using Rhinoceros®.
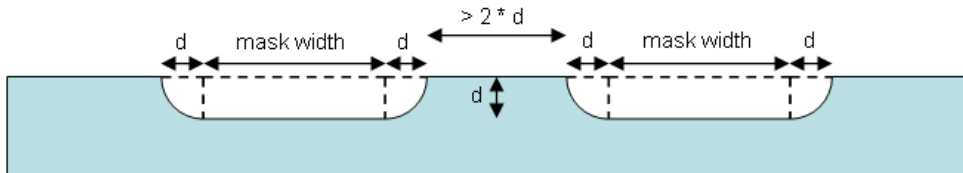
Figure 4-3 – Cross sectional view of channels and pore networks documented by Micronit. Channel depth (d) is 20 μm.

Table 4-2 – Measured dimensions and calculated areal properties for three available network types.

Network Type	Bulk Area [mm²]	Pore Area [mm²]	Bulk Volume [mm³]	Pore Volume [mm³]	Areal Porosity [%]	Volumetric Porosity [%]
Uniform	201.406	120.447	4.028	2.100	59.8	52.1
Random	198.390	86.996	3.968	1.600	43.8	40.3
Physical Rock	200.398	125.001	4.008	2.300	62.4	57.4

4.1.2 Absolute Permeability Calculation

Absolute permeability is calculated by applying Darcy equation for horizontal incompressible single-phase flow:

$$u_D = -\frac{K_{abs}}{\mu}\nabla P \tag{4.1}$$

where u_D, K_{abs}, μ and ∇P are Darcy velocity, absolute permeability, viscosity and pressure gradient, respectively. Furthermore, Darcy velocity can be written as:

$$u_D = \frac{q}{A} \tag{4.2}$$

where q is the flow rate and A is the cross sectional area of the micromodel. Substituting equation (4.2) in equation (4.1) and a simple rearrangement gives:

$$K_{abs} = -\frac{qL\mu}{A\Delta P} \tag{4.3}$$

where L is the length of porous network. All required parameters for calculating absolute permeability in equation (4.3) are available as will be explained in the following.

General setup for microfluidic experiments is shown in Figure 4-1. In order to calculate the absolute permeability of the chips, distilled water was used since it can be considered as an incompressible fluid with a viscosity of 1 cp at 25°C. The procedure is as follows:

1) Air contained in the system (i.e. micromodel and lines) is removed using vacuum pump or high pressure injection

2) The system is saturated with distilled water. The pump, lines and the microchip must be inspected to be free of air bubbles.

3) Injecting distilled water into the saturated system and recording the differential pressure. Three to four runs with different flow rates are performed for each micromodel. This provides results that are more reliable and assists in finding the system offset. The injection continues until steady state condition is reached.

Next step is to read the average differential pressure at steady state condition from the recorded pressure graphs. Figure 4-4 shows an example of recorded pressure graph. By plotting the differential pressure versus flow rate, linear relationship between data points can be established (Figure 4-5). The slope and the intercept of each dataset trend line represent $\Delta P/q$ and the system offset, respectively. Table 4-3 presents the calculated absolute permeability for each microchip.
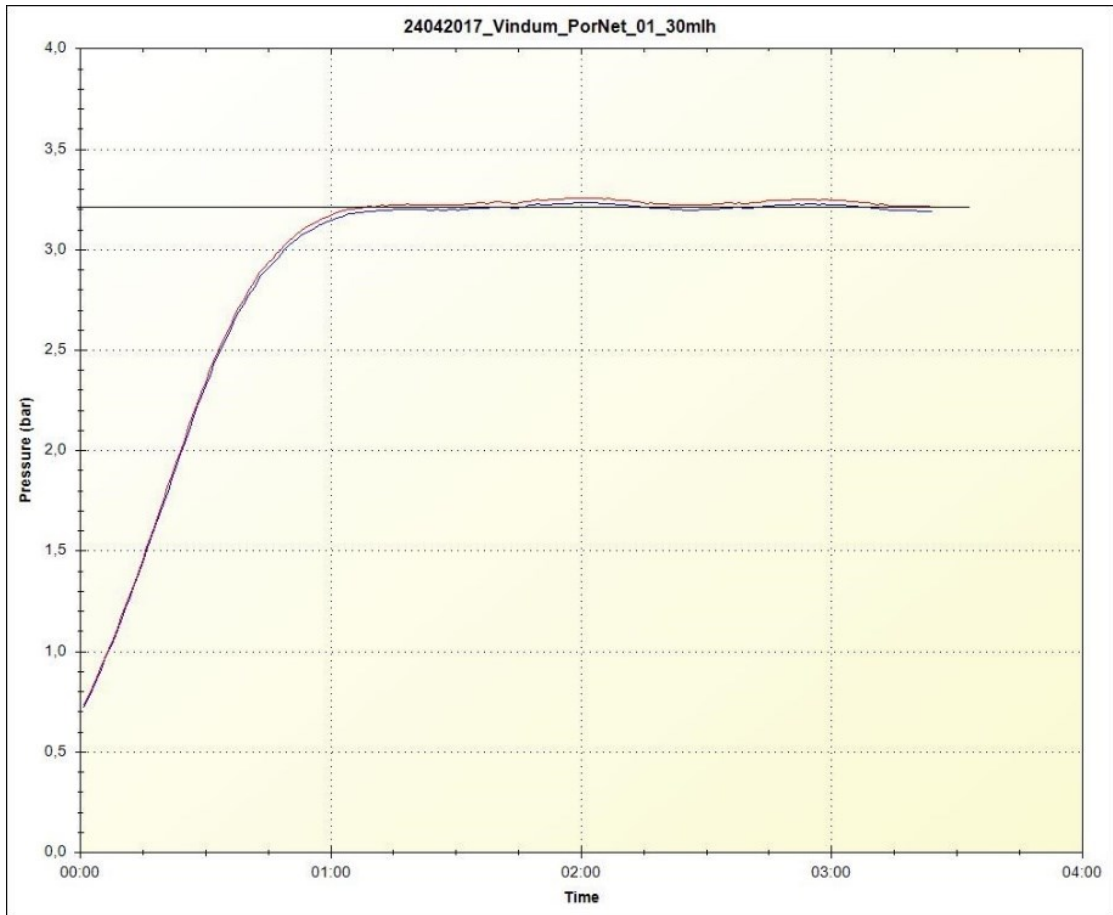
Figure 4-4 – Average differential pressure at steady state conditions can be read (black line) from recorded pressure graphs.

Table 4-3 – Calculated absolute permeability for different rock networks.

Network Type	Porous Medium Width [cm]	Porous Medium Depth [cm]	Porous Medium Length [cm]	Viscosity of Water at 25°C [cp]	System Offset [bar]	Average System Offset [bar]	Absolute Permeability [D]
Uniform	1.009	0.002	1.996	1	0.08		2.57
Random	1.004	0.002	1.976	1	0.08	0.08	1.42
Physical Rock	1.004	0.002	1.996	1	0.08		2.53
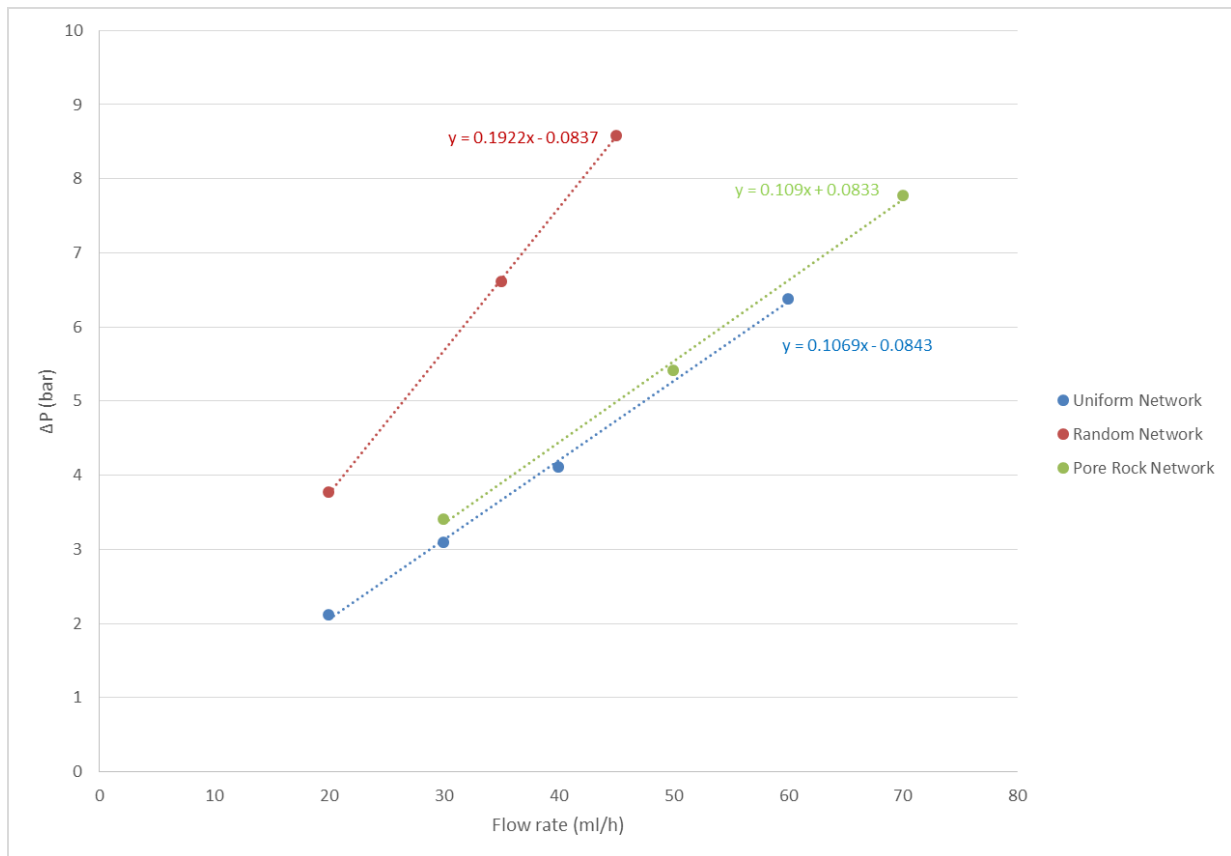
Figure 4-5 – Plotted flow rate vs. differential pressure for three different microchips

4.2   Microfluidic Chips Cleaning Procedure

To make sure that microfluidic experimental results are reliable and reproducible, establishing a proper cleaning procedure is of extreme importance. The cleaning technique developed and implemented in the overall workflow is as follows:

1. First step is to inject 250 pore volumes (or more) of distilled water at high pressure. The maximum allowable pressure in experiments performed in this thesis is below 15 bars since the three-way connection valves started to leak at higher pressures.

2. Injection of 50 pore volumes (almost 1 ml) isopropyl alcohol[5] or acetone[6] and providing an efficient soaking time for the system (30 – 60 minutes). Under this time, the acetone should be able to mix with remaining water in dead-end pores and react with crude residuals to some extent.

3. Flooding the microchip with 50 – 100 pore volume toluene[7] for 3 – 4 hours until no traces of oil is observed (under microscope).

4. Repeating step 2 with acetone.

5. Evaporating the acetone by injecting air until no trace of acetone is visible.

---

[5] C_3H_7OH

[6] $(CH_3)_2CO$

[7] $C_6H_5CH_3$

4.3   Photo Capturing and Full Range Image Preparation

As schematically shown in Figure 4-1, during the flood experiments, digital images of microfluidic chip were captured in 30 – 90 seconds intervals by the aid of a microscope and a digital camera. As previously mentioned, due to limitation of the available microscope, it was not possible to capture the full range images of micromodel (Figure 4-6). To make the images of different experiments comparable, attempts were made to capture the same location of the microchip.

At the end of each experiment, the camera of the pendant drop device (available in the laboratory) was used to capture photos covering larger areas of the microchip (Figure 4-7). Since the device has a precise digitally controllable x-y table, it was possible to provide full range images. This was done by capturing photos of different areas and stitch them together using a photo editing software. (Figure 4-8).
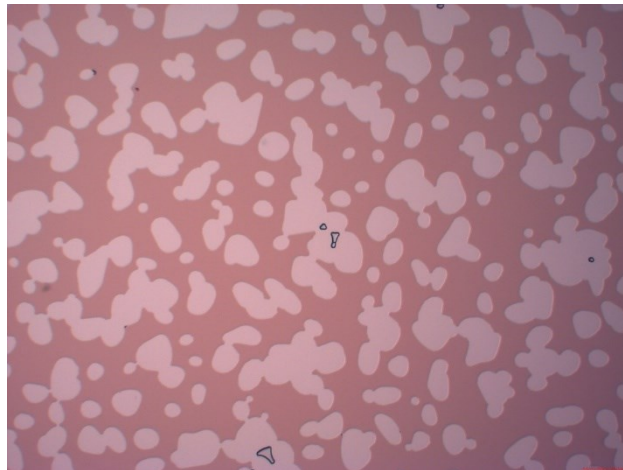

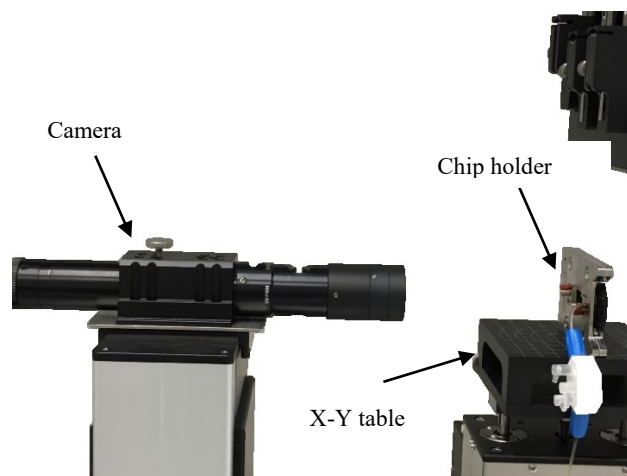*Figure 4-6 – Captured image using microscope (the microchip is saturated with oil).*

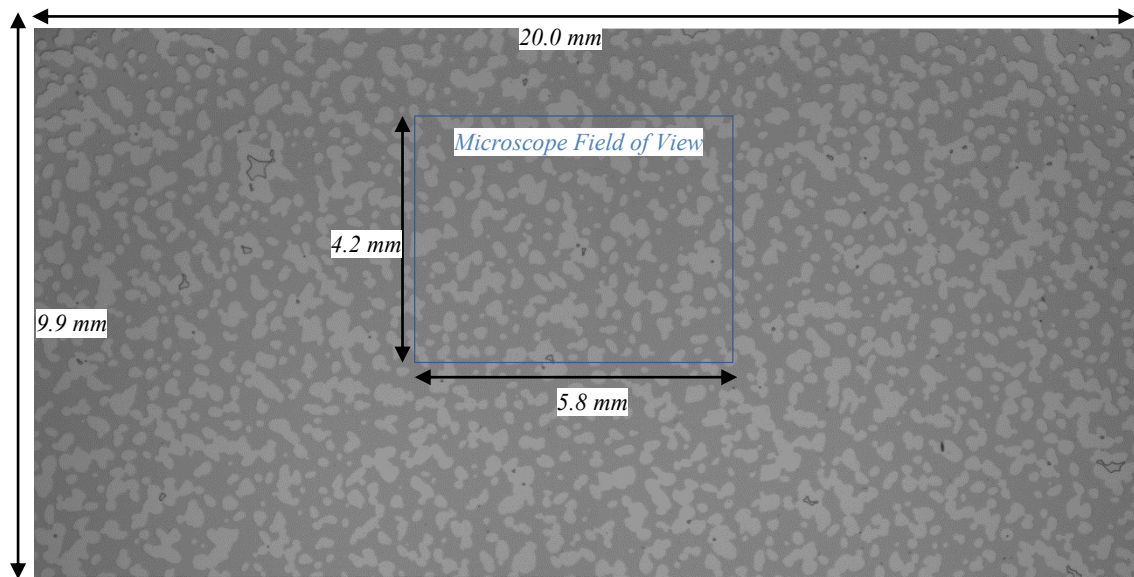*Figure 4-7 – Providing full range pictures using pendant drop device.*

Figure 4-8 – prepared full range image (the microchip is saturated with oil).

4.4 Image Analysis

In order to calculate the recovery factor of the flooding experiments, images had to be analyzed. Recovery factor can be easily calculated by counting the number of pixels representing the residual/remaining oil in binary (black and white) images. Since the contrast between the oil and water is high in the obtained images, it is possible to differentiate the two phases by defining a proper threshold range and convert them to binary images. In the following, the implemented image analysis and validation procedures are explained briefly.

The software "ImageJ" was used as the image-analysis tool in this research. The advantages of this application are as follows:

- It is worldwide known and user friendly.
- The software is free and open source.
- Writing macros and automating the analysis processes are possible and very easy to implement.

Before starting with the procedure description, it is worth explaining some important expressions and commands regarding image analysis:

- *Dilate:* adds pixels (white) to the edges of objects in a binary image.
- *Erode:* removes pixels (white) from the edges of objects in a binary image.
- *Subtract Background:* removes smooth continuous backgrounds from images. This feature is very useful when analyzing images with an uneven background light distribution. (Figure 4-9)
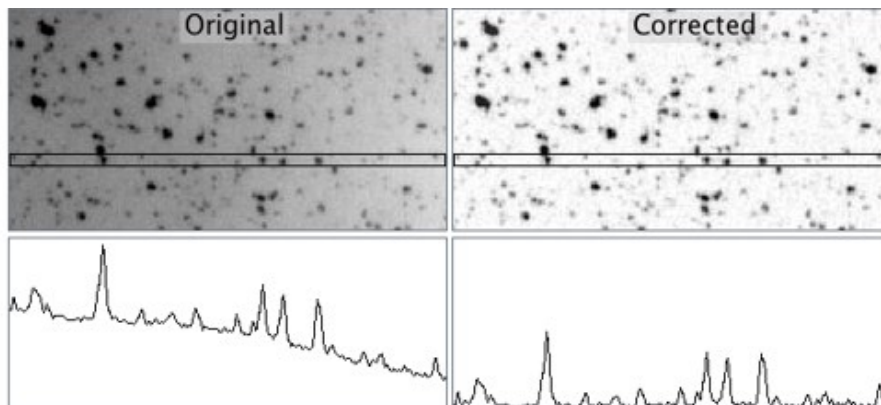
Figure 4-9 – Illustration of "rolling ball" algorithm background remover (ImageJ User Guide).

4.4.1 Image Analysis Procedure

To validate the results of image processing procedure, images of both 100% oil saturated and 100% water saturated microchips were processed. The measured areal porosity were compared with the one calculated in section 4.1.1.

4.4.1.1 Areal Porosity Measurement Using Oil Saturated Microchip Image

As a starting point, color channels are split. This results in 3 individual channel images: red, green and blue. Then the background has to be subtracted, as the background light is not evenly distributed and gives rise to creating improper binary images. The final step is to adjust the black and white threshold values in order to achieve a suitable binary image. The values can be found by trial and error method. For intact oil, a black range with a lower limit value of 247 and an upper limit of 255 produced reasonable results based on available images, however, in some images significant errors were observed. It is always recommended to double check the images that were not captured in exactly similar conditions (such as light, chip holder position, etc). Two times "Dilate" and two times "Erode" is applied to diminish the visible artifacts. In binary images, the ratio of the white pixels (representing oil in this case) to the black pixels (representing grains) can be easily measured by using the "measure" command in ImageJ. Since the microchip is saturated with oil, the fractional area (white to black) is equal to the areal porosity, as shown in Figure 4-10. The measured porosity is 62.6%, which shows very good consistency with the one measured in section 4.1.1 (i.e. 62.4%).
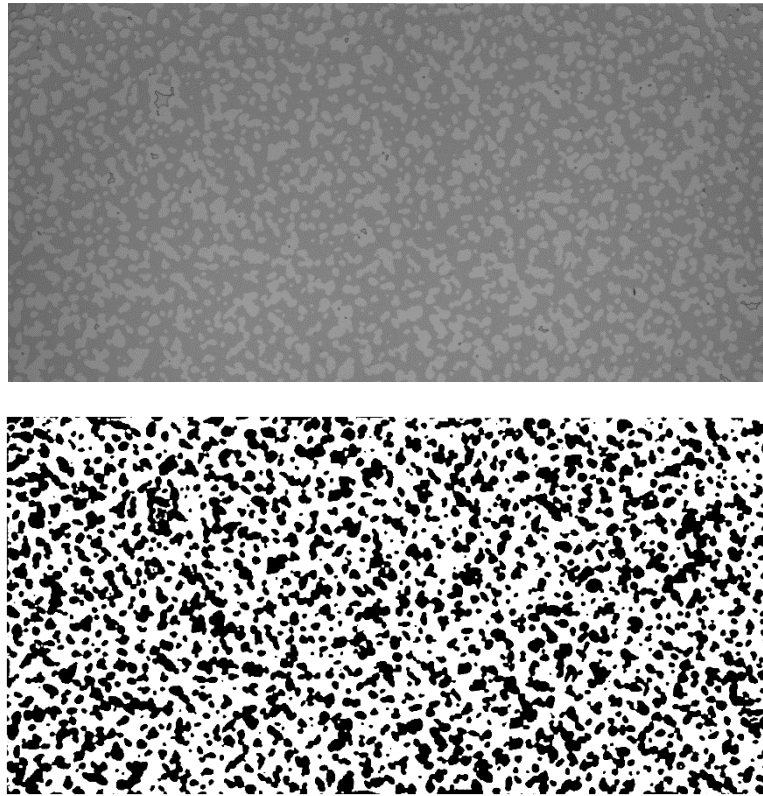
Figure 4-10 – Oil saturated microchip image analysis, (upper) original image (lower) binary image

4.4.1.2 Areal Porosity Measurement Using Water Saturated Microchip Image

The image of the 100% water saturated microchip was analyzed to calculate the areal porosity. As can be seen in Figure 4-11, grain areas and areas saturated with water appear in white range and boundaries of grains are captured as black lines. Analyzing the binary image of a fully water-saturated microchip yielded a ratio of approximately 18 % black to white pixels. It is necessary to define whether these boundaries (black lines) have to be considered as part of the grain area or the porous medium. To do so, a simple analysis was performed, in which the inner area of grains in binary image (Figure 4-11) was filled with black color manually. The porosity was then measured and compared with the one calculated based on fully oil saturated micromodel image of the same area. As shown in Figure 4-12, the calculated porosity from the manually filled image provided a value of 45%, which is almost 18%, less than the one determined from the oil-saturated image (63.2%). This indicates that the black lines representing grain boundaries appear in the porous medium and corrections need to be applied for further analyses.
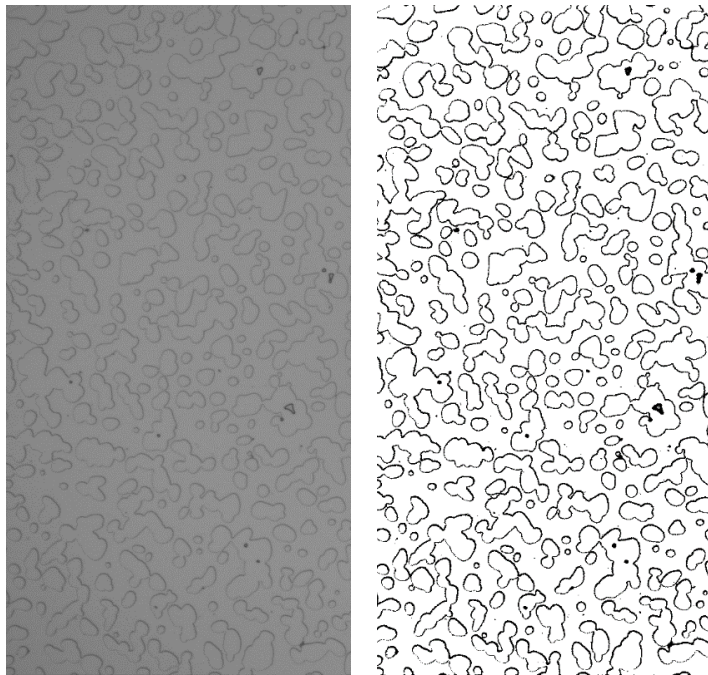
Figure 4-11 – Water saturated microchip image analysis, original image (left) binary image (right).

The correction is done by two times applying "dilate" command, and then two times "erode" command. This reduces the ratio of black to white pixels from 18% to less than 0.5%. On the other hand, this correction does not have any significant effect on the oil-accumulated areas.
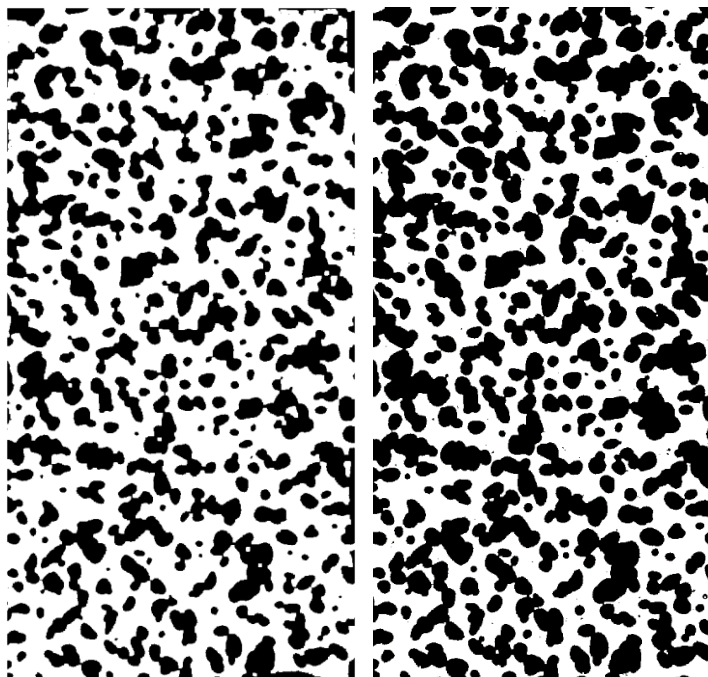
Figure 4-12 – Comparing porosity values calculated using oil saturated model (left), with manually filled grain areas image (right).

4.4.2 Image Analysis Automation

Macros can be easily implemented in ImageJ to automate the image analysis procedure. Automation is required particularly when a large number of images have to be analyzed. In Appendix A, two macros that have been developed and implemented to analyze full-range and microscope-taken images are presented. By running each macro, the user only has to specify the source folder where the images are located and the output folder in which the processed images should be saved. A list with the name of every processed image files and measured white to black pixel ratio will appear in a "Result window".

4.5   Alkaline Flooding Experiments

This section presents the general procedure of the flooding experiments that was developed for this study. Microchips with "physical rock" pore network were used to investigate the effects of alkaline flooding on oil recovery under secondary and tertiary recovery modes utilizing oil samples from three different reservoirs located in Austria supplied by OMV. All experiments were conducted under ambient temperature.

4.5.1 Oil Samples and Their Properties

The Matzen oil field is located 20 km northeast of Vienna in the Vienna basin, which consists of many reservoirs (Gruenwalder et al. 2007). The 8th and 16th Torton Horizon (TH) reservoirs are the two main prolific horizons of the Matzen field, which are under investigation for future alkaline flooding. Oil samples from 8th and 16th Torton reservoirs were supplied by OMV. Both samples are characterized with high viscosity and TAN value. Additionally, a light oil sample from St. Ulrich – Flysch reservoir was provided, which enabled us to study the effects of alkaline flooding on a low TAN sample. In Table 4-4, relevant properties of the oil samples are summarized.

4.5.2 Experimental Procedure

Sodium hydroxide and sodium carbonate are the two most common types of alkaline salts used for EOR purposes. In this thesis, deionized water was utilized as the solvent to provide alkaline solutions. Salinity and other impurities were kept at zero to narrow down the range of influencing variables. Only alkaline type and concentration were considered as adjustable parameters. Injection rate for all the experiments was set to be 0.01 ml/h. The pH of the solution was measured using pH indicator strips. Alkaline solutions were injected as secondary and tertiary recovery modes. For the secondary recovery experiments, microchips were initially

fully saturated with oil followed by the injection of alkaline solution into the system. To conduct tertiary recovery experiments, the microchip was first saturated with oil and then flooded with distilled water until no further oil recovery was observed (for approximately 24 hours). Thereafter, the alkaline solution was injected and data gathering was done as previously explained in section 4.4. Table 4-5 presents the details of each experiment.

Table 4-4 – Oil samples properties

	Oil Sample 1	Oil Sample 2	Oil Sample 3
Well	Schönkirchen 446	Bockfliess 112	St. Ulrich 65
Reservoir	8th Torton Horizon	16th Torton Horizon	Flysch
Sampling date	17.11.2015	19.10.2016	09.02.2017
Sample-ID	CHE20155426	CHE20165728	CHE20170827
TAN [mg KOH/g oil]	1.96	1.56	0.34
Density @ 20 °C [g/cm³]	0.9306	0.9070	0.8711
Density @ 15 °C [g/cm³]	0.9339	0.9104	0.8746
Viscosity @ 20 °C [cP]	331	80	-
API °(8)	19.88	23.79	30.14

---

[8] Density of water at 15 °C is 0.9991 g/cm³

Table 4-5 – Details of alkaline flooding experiments

	Oil Sample	Alkaline Type	Alkalinity [mmol/l] / Alkaline Concentration [ppm]	Solution pH	Secondary Flood	Tertiary Flood
Exp. 1-1-1	8th TH	-	Deionized Water	7	✓	✗
Exp. 1-1-2	8th TH	-	Deionized Water	7	✓	✗
Exp. 1-1-3	8th TH	-	Deionized Water	7	✓	✗
Exp. 1-2-1	16th TH	-	Deionized Water	7	✓	✗
Exp. 1-2-2	16th TH	-	Deionized Water	7	✓	✗
Exp. 1-2-3	16th TH	-	Deionized Water	7	✓	✗
Exp. 1-3-1	Flysch	-	Deionized Water	7	✓	✗
Exp. 1-3-2	Flysch	-	Deionized Water	7	✓	✗
Exp. 1-3-3	Flysch	-	Deionized Water	7	✓	✗
Exp. 3	8th TH	Na_2CO_3	18 / 950	10	✓	✗
Exp. 4	16th TH	Na_2CO_3	18 / 950	10	✓	✗
Exp. 5	Flysch	Na_2CO_3	18 / 950	10	✓	✗
Exp. 6	8th TH	NaOH	18 / 720	11	✓	✗
Exp. 7	16th TH	NaOH	18 / 720	11	✓	✗
Exp. 8	Flysch	NaOH	18 / 720	11	✓	✗
Exp. 9	8th TH	Na_2CO_3	18 / 950	10	Exp. 1-1-1	✓
Exp. 10	16th TH	Na_2CO_3	18 / 950	10	Exp. 1-2-1	✓
Exp. 11	Flysch	Na_2CO_3	18 / 950	10	Exp. 1-3-1	✓
Exp. 12	8th TH	NaOH	18 / 720	11	Exp. 1-1-2	✓
Exp. 13	16th TH	NaOH	18 / 720	11	Exp. 1-2-2	✓
Exp. 14	Flysch	NaOH	18 / 720	11	Exp. 1-3-2	✓
Exp. 15	8th TH	Na_2CO_3	226 / 12000	12	Exp. 1-1-3	✓
Exp. 16	16th TH	Na_2CO_3	226 / 12000	12	Exp. 1-2-3	✓
Exp. 17	Flysch	Na_2CO_3	226 / 12000	12	Exp. 1-3-3	✓

<div align="right"># Chapter 5</div>

Results and Discussion

This chapter presents observations, findings and results of the previously described alkaline flooding experiments. In each experiment, ultimate residual oil saturation was measured by analyzing the full-range images and recovery factors were calculated. Data originating from microscope taken images were used to plot recovery and oil saturation curves.

5.1 Average Ultimate Recovery Factor and Observations

The average recovery factor for alkaline flooding experiments was calculated using the following equation:

$$RF = \frac{volume\ of\ produced\ oil}{volume\ of\ oil\ intially\ in\ place} = \left(1 - \frac{A_{oil-residual}}{A_{oil-initial}}\right) \times 100 \qquad (5.1)$$

Where RF, $A_{oil-residual}$ and $A_{oil-saturated\ model}$ are recovery factor [%], fractional area covered by oil and fractional area covered by oil at initial condition (i.e. before secondary flood), respectively.

Table 5-1 presents the determined recovery factors for the different experimental scenarios. The following observations were drawn from this table:

- For each oil sample, 3 waterflood experiments were performed. As the table shows, for experiments 1-1-1, 1-1-2 and 1-1-3, the 8th TH oil sample was used. Likewise, for experiments 1-2-1, 1-2-2 and 1-2-3, the 16th TH oil sample and for experiments 1-3-1, 1-3-2 and 1-3-3 the Flysh oil sample was implemented.
- Among all 9 performed distilled waterflood experiments (experiments 1-1-1 to 1-3-3), the Flysch reservoir oil sample (experiments 1-3-1, 1-3-2) yielded the highest recovery (average of 70%). Experiment 1-3-3 showed a lower recovery compared to experiments

1-3-1 and 1-3-2. The reason behind seems to be a secondary migration of oil remaining in the inlet tube. This problem could be avoided by designing and implementing microchips with two or more separated inlet channels. The more favorable mobility ratio explains the high water recovery of the Flysch oil since it had lower viscosity than the other two samples (Table 4-4). For 8th TH and 16th TH oil samples, almost similar waterflood recovery was reached; however, it is noticeably lower than the reached recovery of the Flysch oil sample. The recovery factor of experiment 1-2-1 was 44%. The underlying reason for this low value (compared to experiments 1-2-2 and 1-2-3) is the lower total injected volume of water. Since the determined recovery factors for experiments 1-2-1 and 1-3-3 are not representative, they are excluded from the average recovery calculations (Table 5-1). Figure 5-1, Figure 5-2 and Figure 5-3 illustrate the original, full-range and processed images of distilled waterflood experiments for the three available oil samples.

- Figure 5-4 shows the processed images of waterflood experiments that were performed for 8th TH, 16th TH and Flysch oil samples. Large oil cluster sizes are observed in the 8th TH (Figure 5-4a) and 16th TH (Figure 5-4b) images compared to the water flooded Flysch sample (Figure 5-4c). Furthermore, Figure 5-4a and Figure 5-4c show a more homogeneous distribution of oil clusters while a very large cluster can be seen in 16th TH (Figure 5-4b) sample image, which extends almost from the inlet (left) to the outlet (right) of microchip. Residual oil saturation for both 8th TH and 16th TH samples are similar (about 45%) while for the Flysch oil sample is measured to be 28%.

- Each experiment mentioned in the previous paragraphs, was followed by a tertiary alkaline flood (see Table 5-1). The respective processed images are presented in Figure 5-5. As a consequence of the applied EOR treatment, the longest oil clusters were broken up and resulted in the formation of smaller clusters (well illustrated by the comparison of Figure 5-4a Figure 5-5a). However, the distribution of residual oil is similar in both cases. Figure 5-5b shows a significant change in the size of the major oil clusters that was indicated in Figure 5-4b. Furthermore, in some areas (upper part of the image) larger clusters can be observed after the tertiary flood. Unfortunately, it is not clear whether this cluster size increase is due to the coalescence of smaller oil clusters or secondary migration of oil remaining in the inlet tube. No changes are noticed in oil saturation and cluster size before and after tertiary flood of the Flysch oil sample (compare Figure 5-4c with Figure 5-5c).

- In the microscopic images, a thicker boundary was observed between the water-oil compared to the oil-solid phases, which is helpful to visually distinguish the water

phase from the solid phase. This is illustrated in Figure 5-6, where black arrows show the grains while blue arrows point toward the water drops. Note that for numerical analyses, pore space and grains were segmented and distinguished using the 100% oil saturated state.

Table 5-1 – Calculated ultimate oil recovery for each experiment

| Experiment	Oil Sample	Alkaline Type	Alkalinity [mmol/l] / Alkaline Concentration [ppm]	Secondary Flood	Tertiary Flood	Recovery Factor [%]	Average Recovery [%]
Exp. 1-1-1		-	Deionized Water	✓	✗	52	
Exp. 1-1-2	8th TH	-	Deionized Water	✓	✗	54	53
Exp. 1-1-3		-	Deionized Water	✓	✗	52	
Exp. 1-2-1		-	Deionized Water	✓	✗	44	
Exp. 1-2-2	16th TH	-	Deionized Water	✓	✗	56	55
Exp. 1-2-3		-	Deionized Water	✓	✗	54	
Exp. 1-3-1		-	Deionized Water	✓	✗	72	
Exp. 1-3-2	Flysch	-	Deionized Water	✓	✗	68	70
Exp. 1-3-3		-	Deionized Water	✓	✗	51	
Exp. 3	8th TH	Na_2CO_3	18 / 950	✓	✗	90	90
Exp. 4	16th TH	Na_2CO_3	18 / 950	✓	✗	71	71
Exp. 5	Flysch	Na_2CO_3	18 / 950	✓	✗	52	52
Exp. 6	8th TH	NaOH	18 / 720	✓	✗	76	76
Exp. 7	16th TH	NaOH	18 / 720	✓	✗	63	63
Exp. 8	Flysch	NaOH	18 / 720	✓	✗	54	54
Exp. 9	8th TH	Na_2CO_3	18 / 950	Exp. 1-1-1	✓	78	78
Exp. 10	16th TH	Na_2CO_3	18 / 950	Exp. 1-2-1	✓	46	46
Exp. 11	Flysch	Na_2CO_3	18 / 950	Exp. 1-3-1	✓	71	71
Exp. 12	8th TH	NaOH	18 / 720	Exp. 1-1-2	✓	58	58
Exp. 13	16th TH	NaOH	18 / 720	Exp. 1-2-2	✓	58	58
Exp. 14	Flysch	NaOH	18 / 720	Exp. 1-3-2	✓	58	58
Exp. 15	8th TH	Na_2CO_3	226 / 12000	Exp. 1-1-3	✓	60	60
Exp. 16	16th TH	Na_2CO_3	226 / 12000	Exp. 1-2-3	✓	63	63
Exp. 17	Flysch	Na_2CO_3	226 / 12000	Exp. 1-3-3	✓	70	70
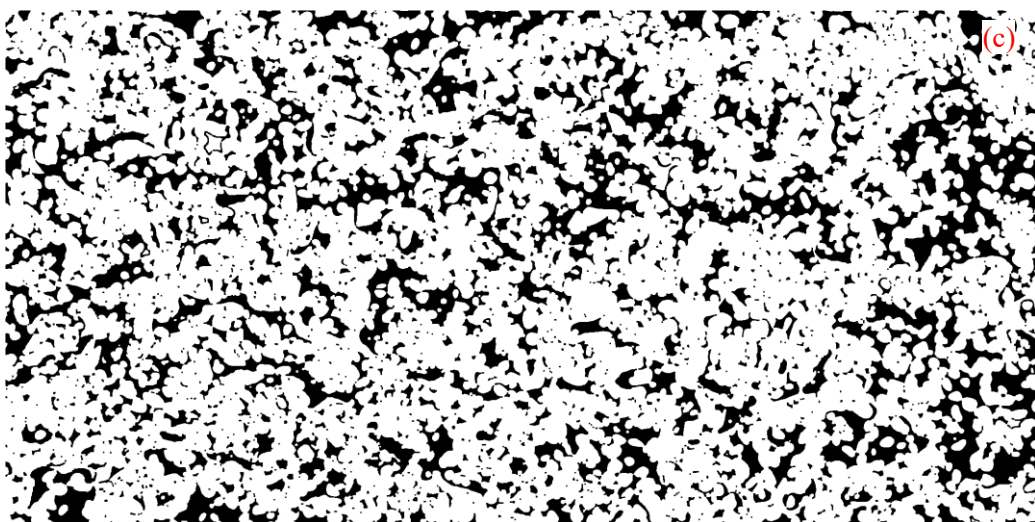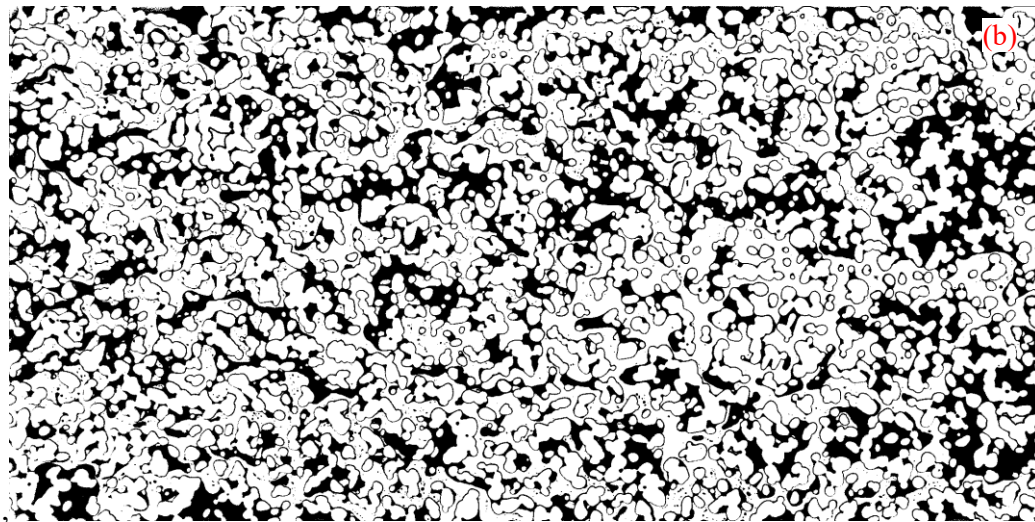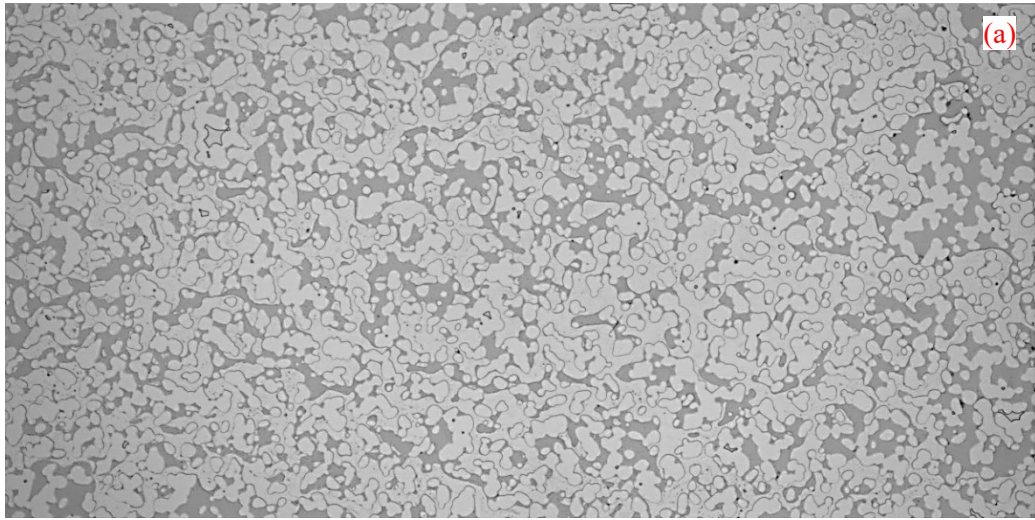
Figure 5-1 – a) Original, b) raw processed and c) final processed full-range images showing residual oil distribution at the end of experiment 1-1-2 (8th TH oil sample flooded with distilled water).
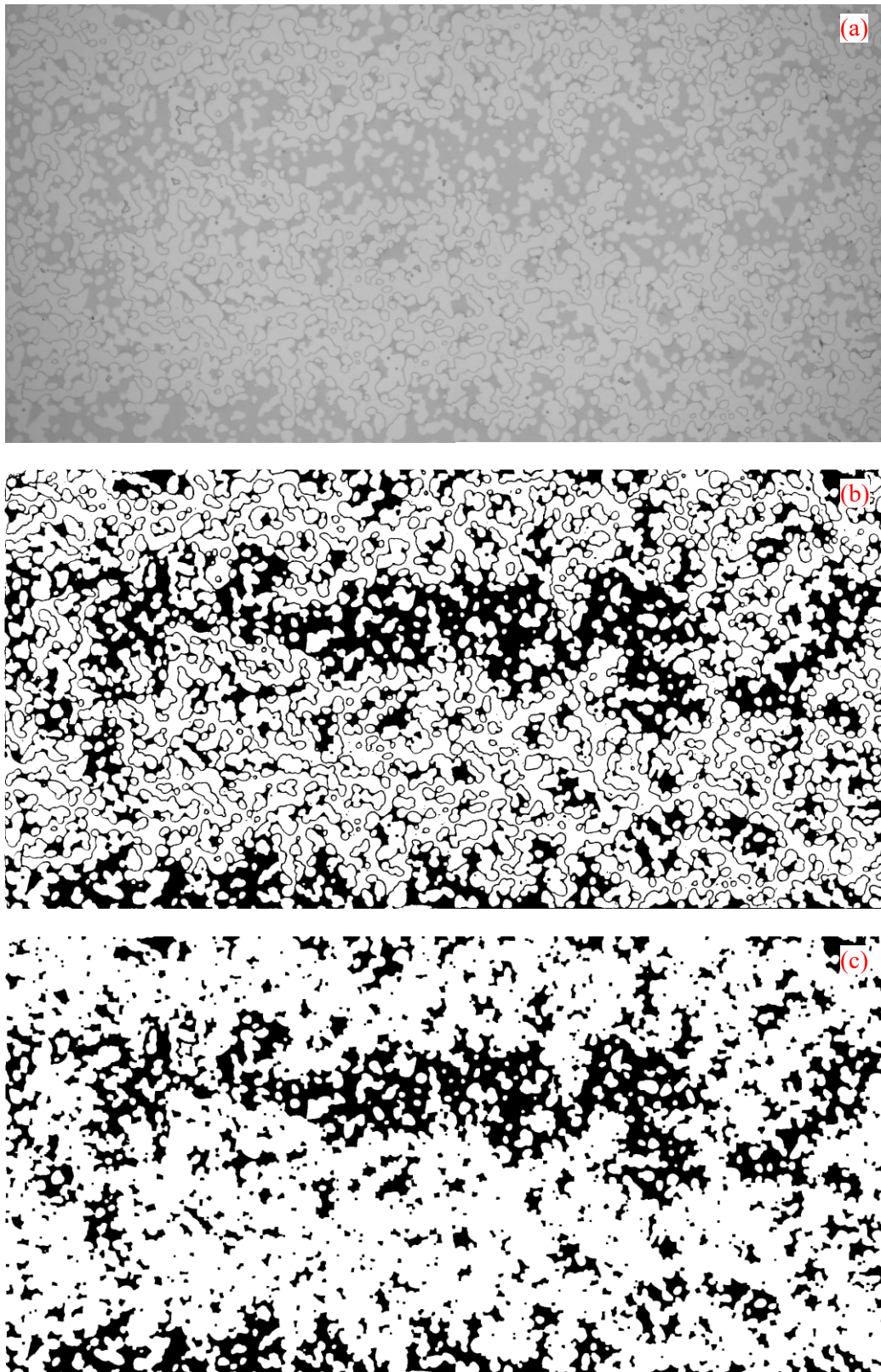
Figure 5-2 – a) Original, b) raw processed and c) final processed full-range images showing residual oil distribution at the end of experiment 1-2-2 (16th TH oil sample flooded with distilled water).
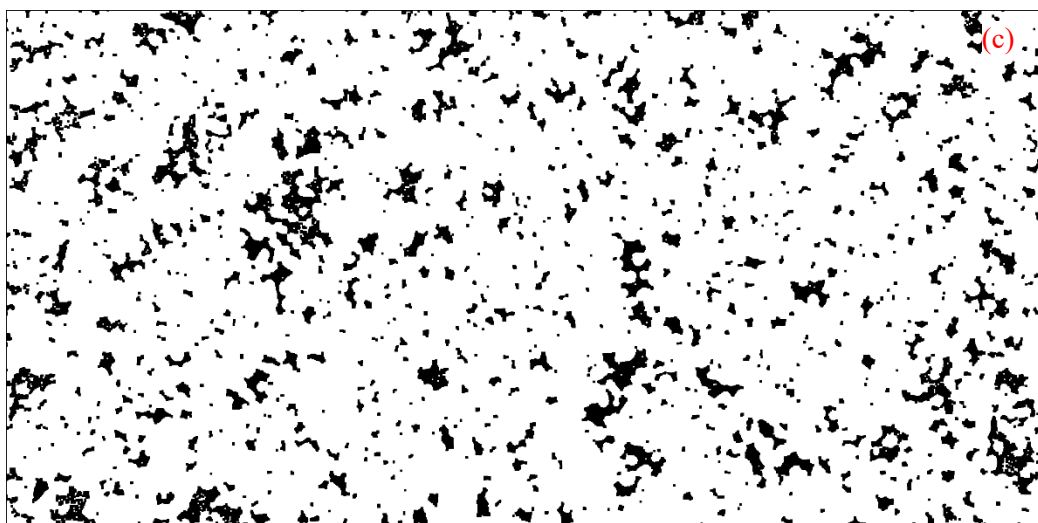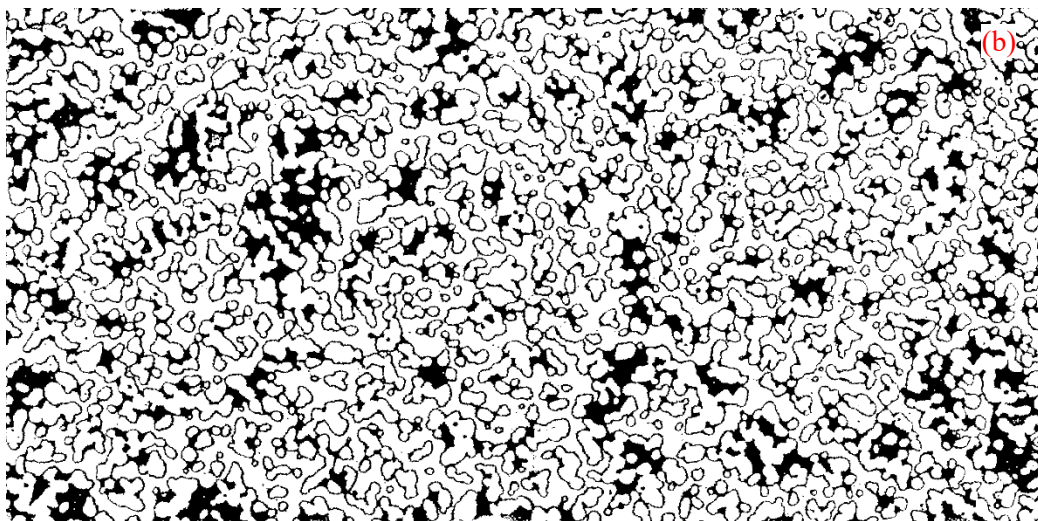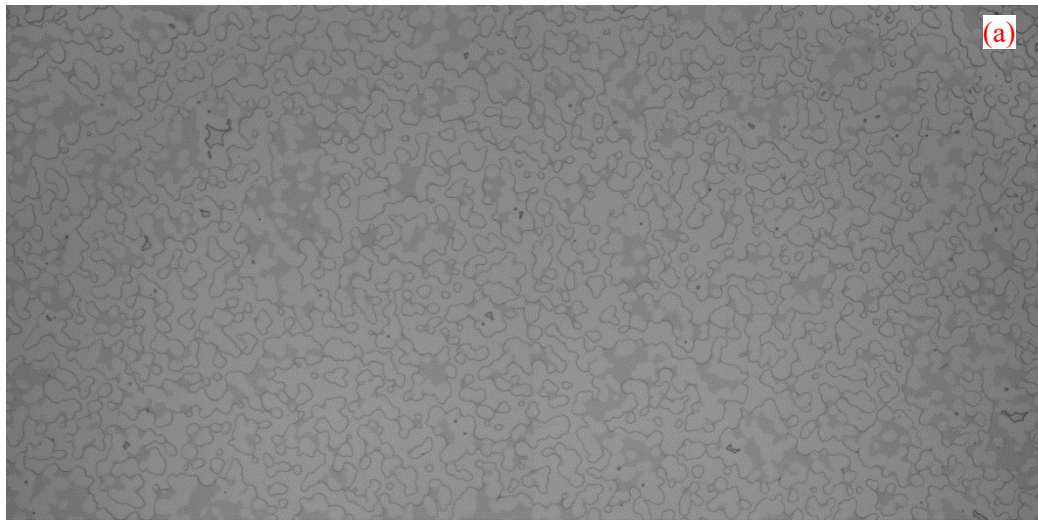
Figure 5-3 – a) Original, b) raw processed and c) final processed full-range images showing residual oil distribution at the end of experiment 1-3-1 (Flysch oil sample flooded with distilled water).

Figure 5-4 – Processed images of a) 8th TH (experiment 1-1-2) b) 16th TH (experiment 1-2-2) and c) Flysch (experiment 1-3-1) oil samples flooded with distilled water.
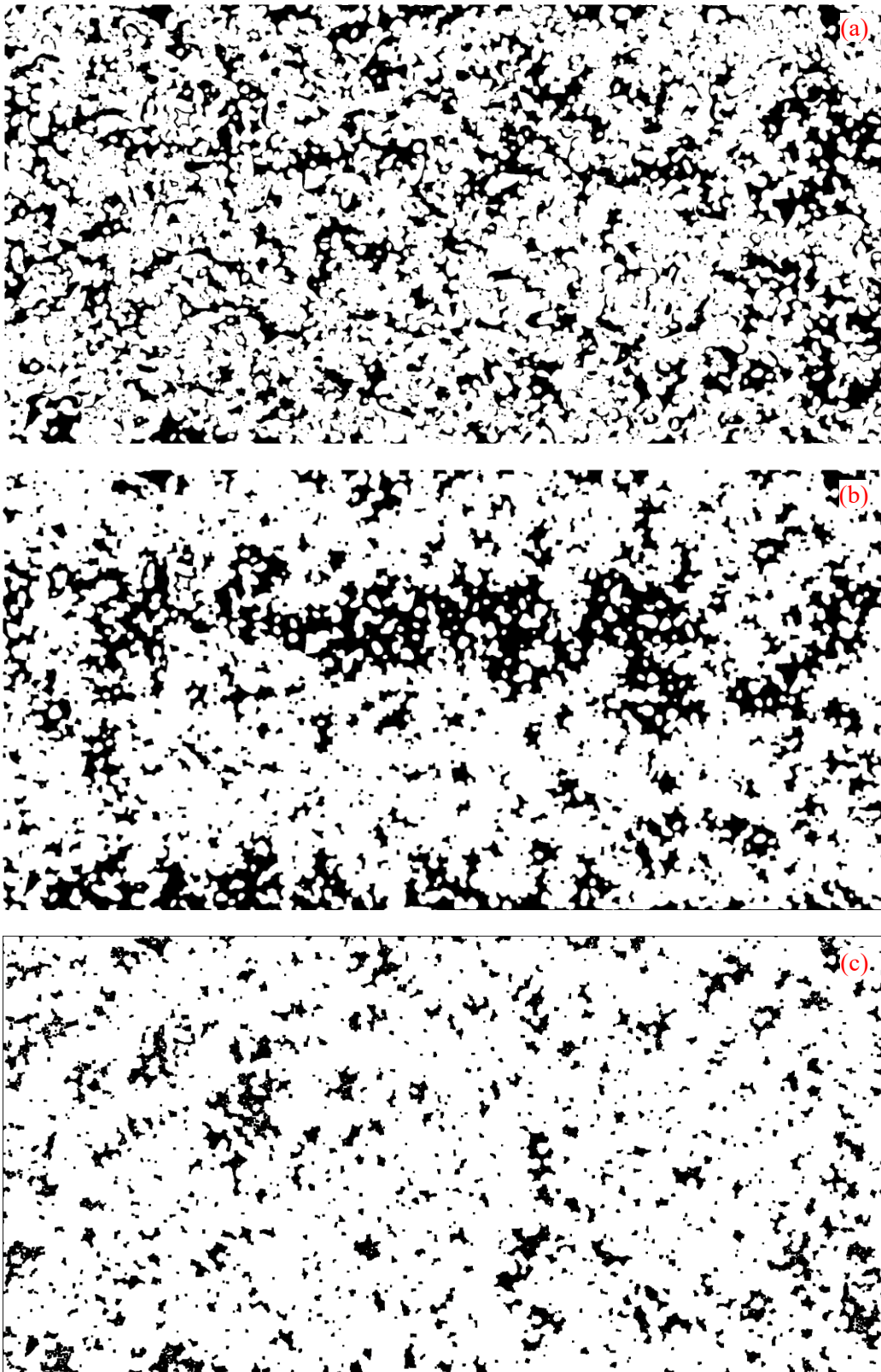
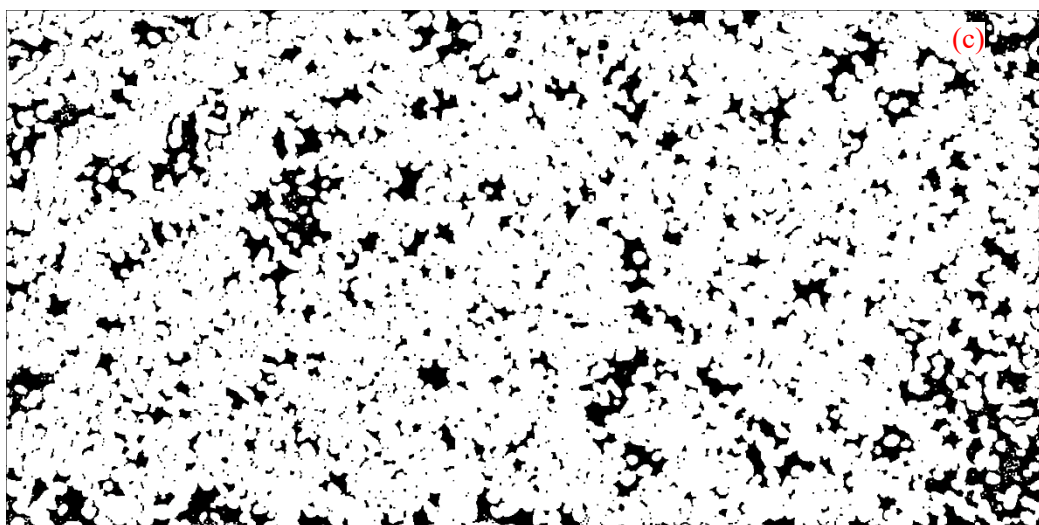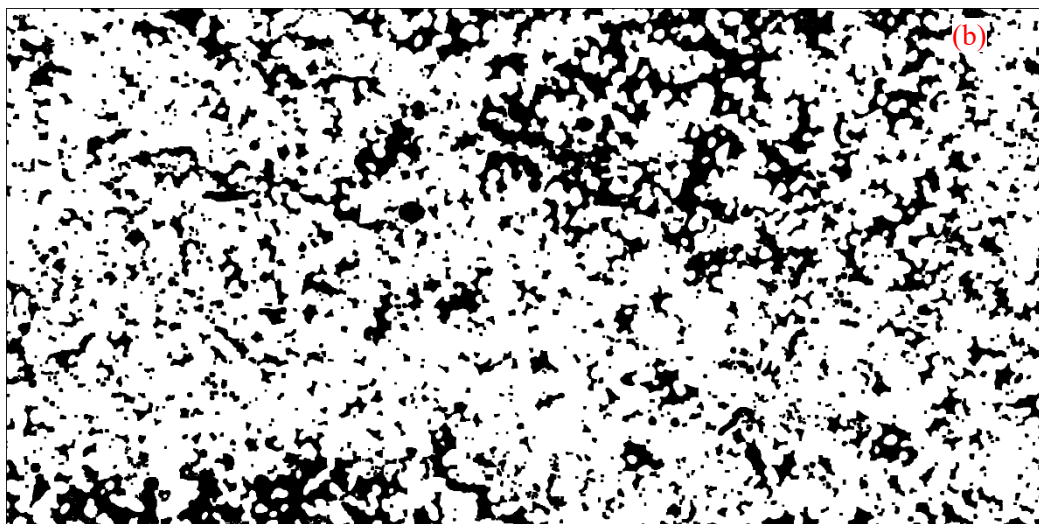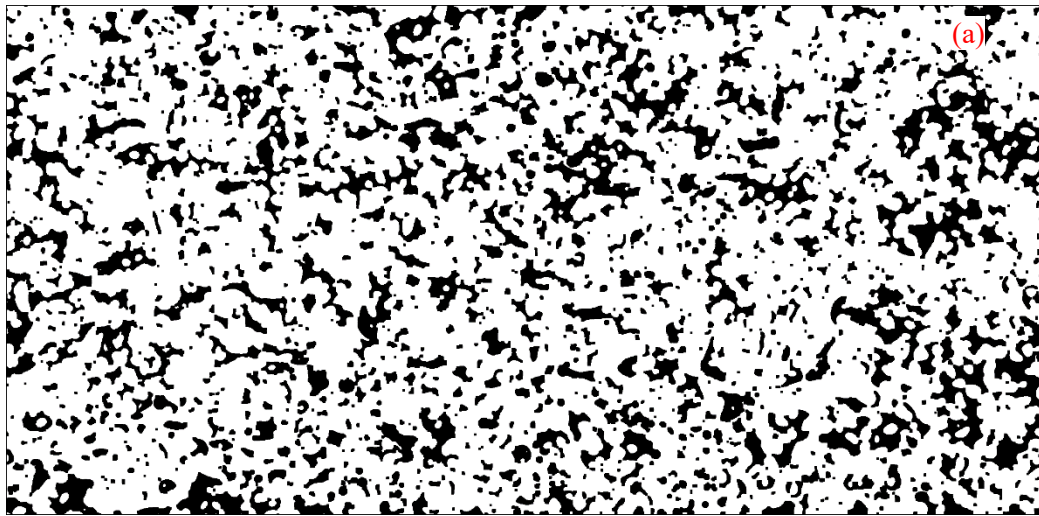*Figure 5-5 – Processed images of a) 8th TH (experiment 12) b) 16th TH (experiment 13) and c) Flysch (experiment 11) oil samples flooded with alkaline solution.*
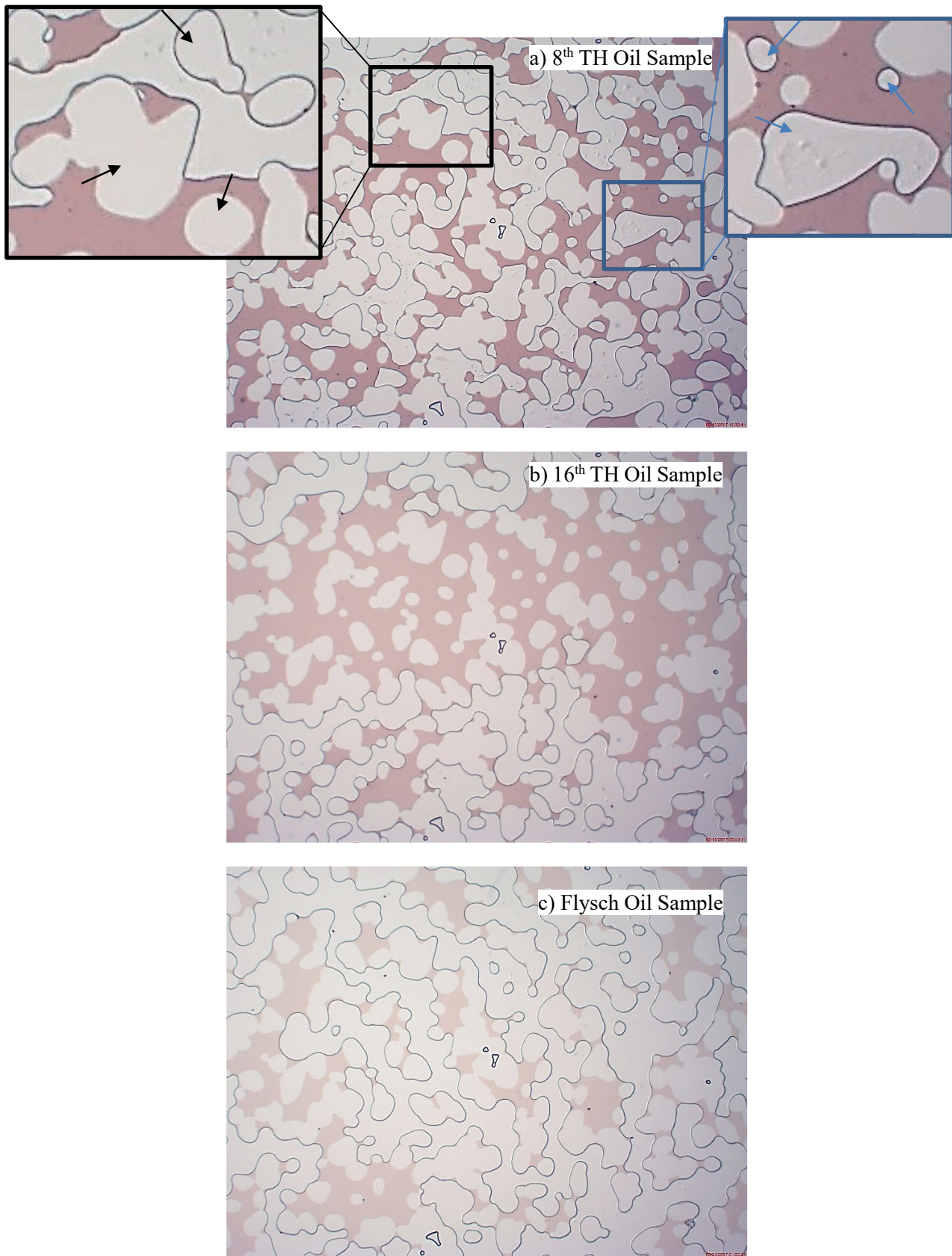
Figure 5-6 – Detailed view (microscopic image) of water (distilled) flood experiments.

- In experiments 3 and 4, the 8th TH and 16th TH oil samples were flooded (secondary) with a 950 ppm Na_2CO_3 solution. By comparing these two experiments, a significantly higher recovery (19% more) for 8th TH sample is observed rather than 16th TH. This is expected because 8th TH has a higher TAN and should therefore be more sensitive to alkaline flooding. Figure 5-7a shows the residual oil saturation after the injection of 950 ppm Na_2CO_3 solution into the microchip saturated with 8th TH oil sample. Lengthy oil clusters were observed (black arrows in Figure 5-7a) for the high TAN case. These clusters have an unfavorable interface to volume ratio and are therefore indicate a low IFT system. As the injection continued, due to shear forces, the tip of the elongated clusters broke off and started to flow within the aqueous phase in the form of oil blobs (red arrows in Figure 5-7a) . This elongation and tip break off was not observed when the same alkaline solution was injected into the 16th TH and Flysch oil samples (Figure 5-7b). This implies that the optimum effective range of alkalinity for different oil samples has to be identified and shows the role of TAN and oil composition on in-situ soap generation.

- Surprisingly, secondary injection of alkaline solutions (either Na_2CO_3 or NaOH) yielded a lower recovery (Experiments 5 and 8) compared to the distilled waterflood experiments in the Flysch oil sample. Furthermore, both type of alkaline solutions showed comparable recoveries.

- Experiments 6 and 7 (flooding 8th TH and 16th TH with 720 ppm NaOH solution) showed lower oil recoveries compared to experiments 3 and 4, respectively. The alkaline solution in these experiments had equal alkalinity but different salinities. Difference in recovery factors as mentioned for these experiments therefore, represents the effect of salinity on the alkaline floods. It is worth mentioning that the pH of the NaOH and Na_2CO_3 solutions were measured to be 11 and 10, respectively (Table 4-5). In Figure 5-8a showing a microscope taken image of experiments 6, the formation of threads of oil was noticed that seems to be a path for oil to flow (shown by black arrows). In contrary to experiment 3, water blobs were detected in the continuous oil phase that might be considered as water-in-oil (W/O) emulsion (marked by blue arrows in Figure 5-8a). No special events were observed experiment 7.
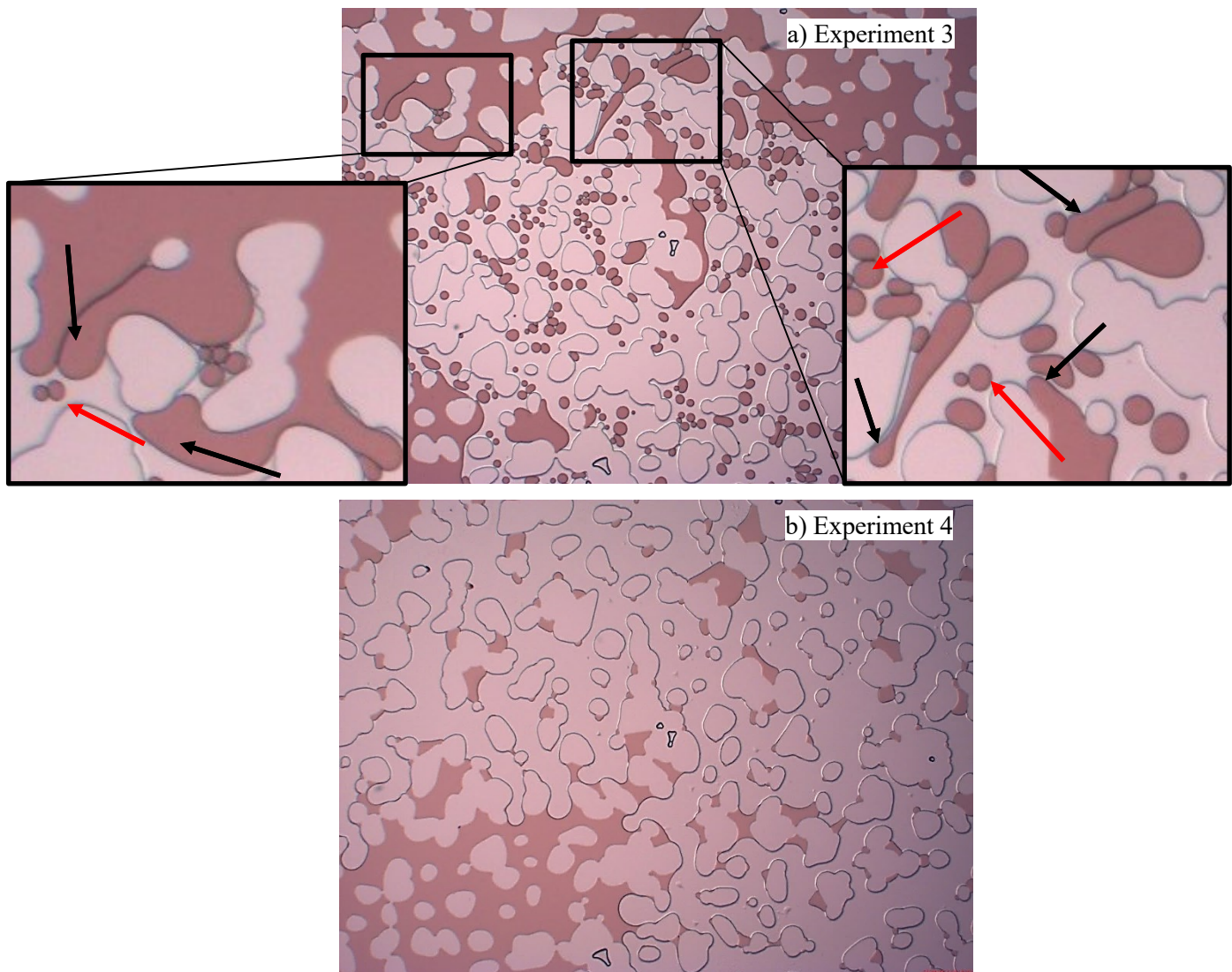
Figure 5-7 – Experiments 3 and 4 microscope taken images

- The injection of alkaline solution as a tertiary flood resulted in the highest incremental recovery (26%) in experiment 9, where the 8th TH oil sample was flooded with 950 ppm Na2CO3 solution. Figure 5-9 presents microscope taken images at different steps of this experiment.

- Flooding 8th TH oil sample with NaOH solution improved the oil recovery only by 4% (experiment 12), and by 8% when 12000 ppm Na_2CO_3 was injected (experiment 15). Only a very limited oil phase elongations and O/W emulsion generation were noted in the microscope taken images of experiment 12 compared to experiment 9.

Figure 5-10 and Figure 5-11 show recorded images of experiment 15 where W/O emulsion with different droplet sizes and oil phase elongations are evident.
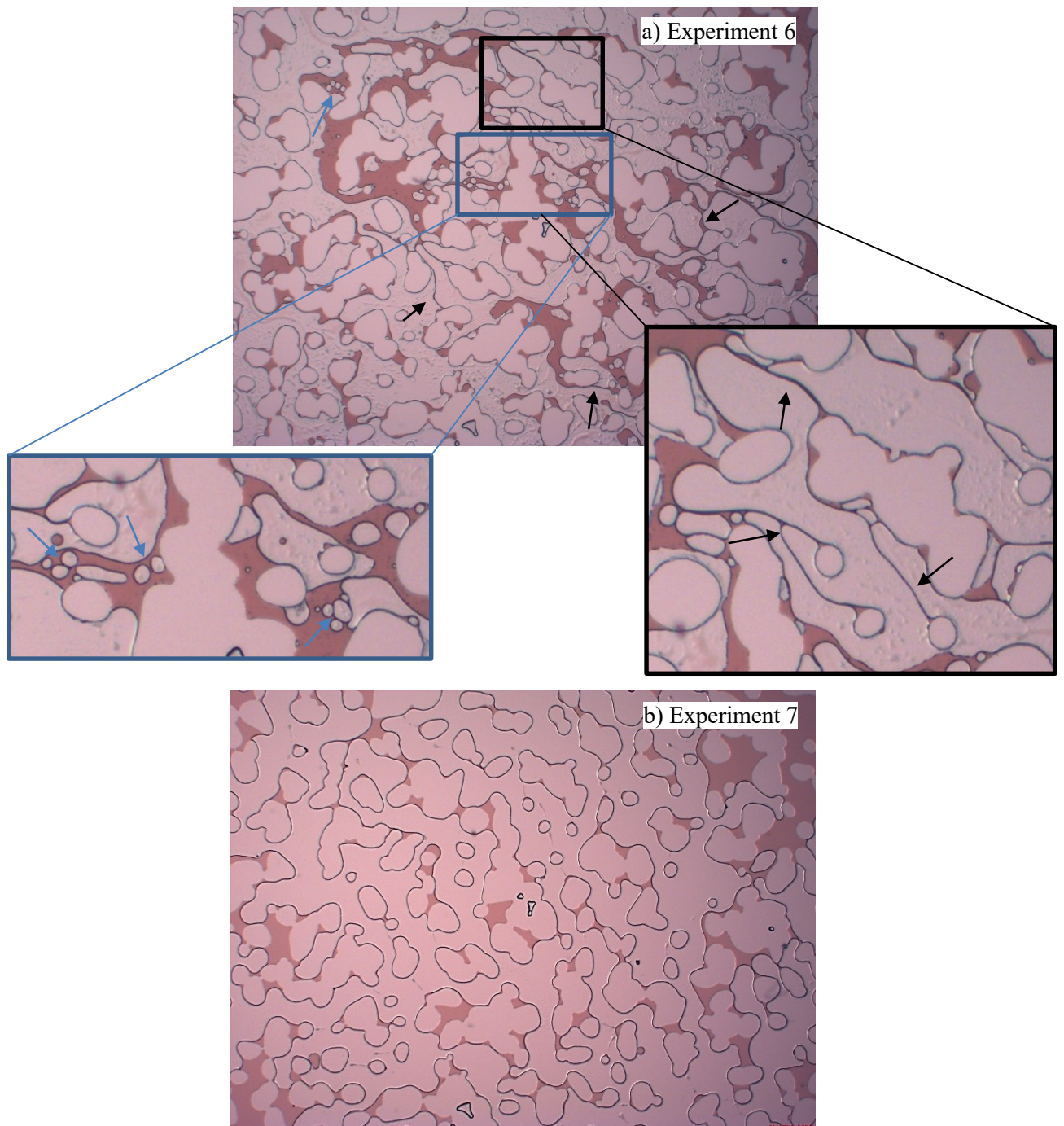
Figure 5-8 – Microscopic images of experiments 6 and 7

- As demonstrated in Figure 5-10c, a dark liquid phase was detected in high-resolution microscopic images that might be interpreted as microemulsion formation. Apart from experiment 15 (Figure 5-10c), this dark phase was also observed in most of the NaOH flooding experiments.

- Experiment 10 (flooding 16th TH oil sample with 950 ppm Na_2CO_3 solution) showed only a 2% recovery enhancement that might also be as a result of image analysis error. Tertiary flooding the same oil sample using 720 ppm NaOH (experiment 13) and 12000 ppm Na_2CO_3 solutions (experiment 16) resulted in 2% and 9% enhanced recovery, respectively.

- In experiment 16, a tertiary alkaline flood experiment was performed on 16th TH oil sample showing noticeable O/W emulsion generation (Figure 5-12 and Figure 5-13). In this case, oil production was advancing even after 24 hours of alkaline solution injection (compare the images with the ones of experiments 3 and 9). Achieving a notably higher amount of recovery is expected with more injection of alkaline solution.

- Tertiary flooding results of Flysch oil sample (low TAN) indicated no changes in average residual oil saturation except in experiment 14 in which a reduction of oil recovery was observed (compared to secondary waterflood recovery in experiment 1-3-2, see Table 5-1). This is probably due to the mobilization of remaining oil in the inlet flow line. As the remaining oil starts to flow and enters the porous medium, it may trap and remain in the microchip. Since the recovery factor is calculated based on residual oil saturation, an increase in residual oil causes a reduction in the calculated oil recovery factor. Therefore, the presented recovery factor of this experiment is not reliable.

- No particular reaction or behavior was observed as the alkaline solutions were injected to Flysch oil sample, which approves the ineffectiveness of such treatments in this low TAN oil sample.

- In general, under similar conditions (e.g. temperature, injection rate, etc.) secondary alkaline injection experiments resulted in much lower ultimate residual oil saturation compared to those experiments where the microchip was first flooded with water and then flooded with alkaline solution (tertiary alkaline injection).
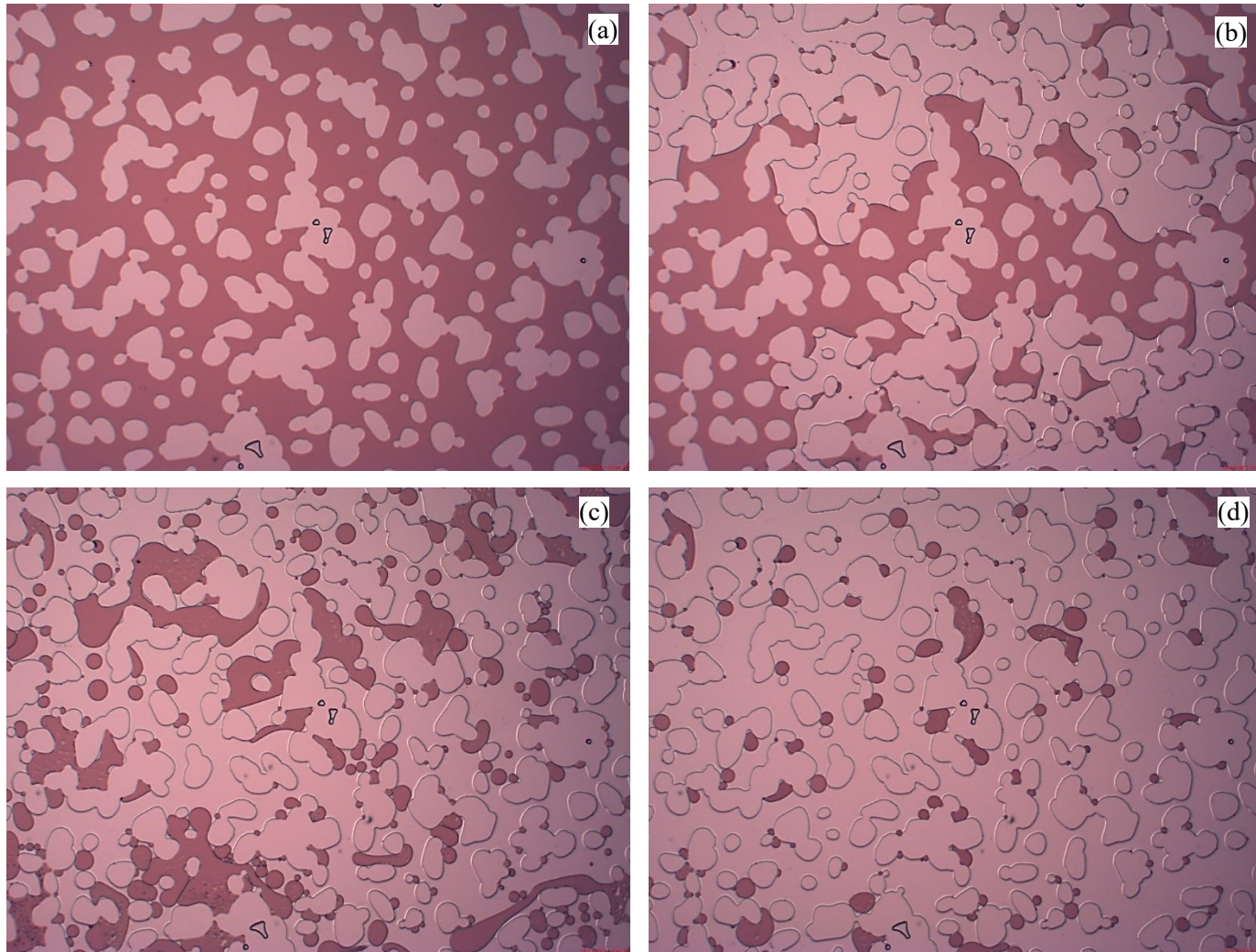
Figure 5-9 – Different steps of experiments 1-1-1 (secondary waterflood) and 9 (tertiary alkaline solution injection). a) Micromodel saturated with 8th TH oil sample, b) oil saturation at the end of distilled waterflood, c) oil phase elongation and O/W emulsion generation during experiment 9, d) residual oil saturation at the end of experiment 9.
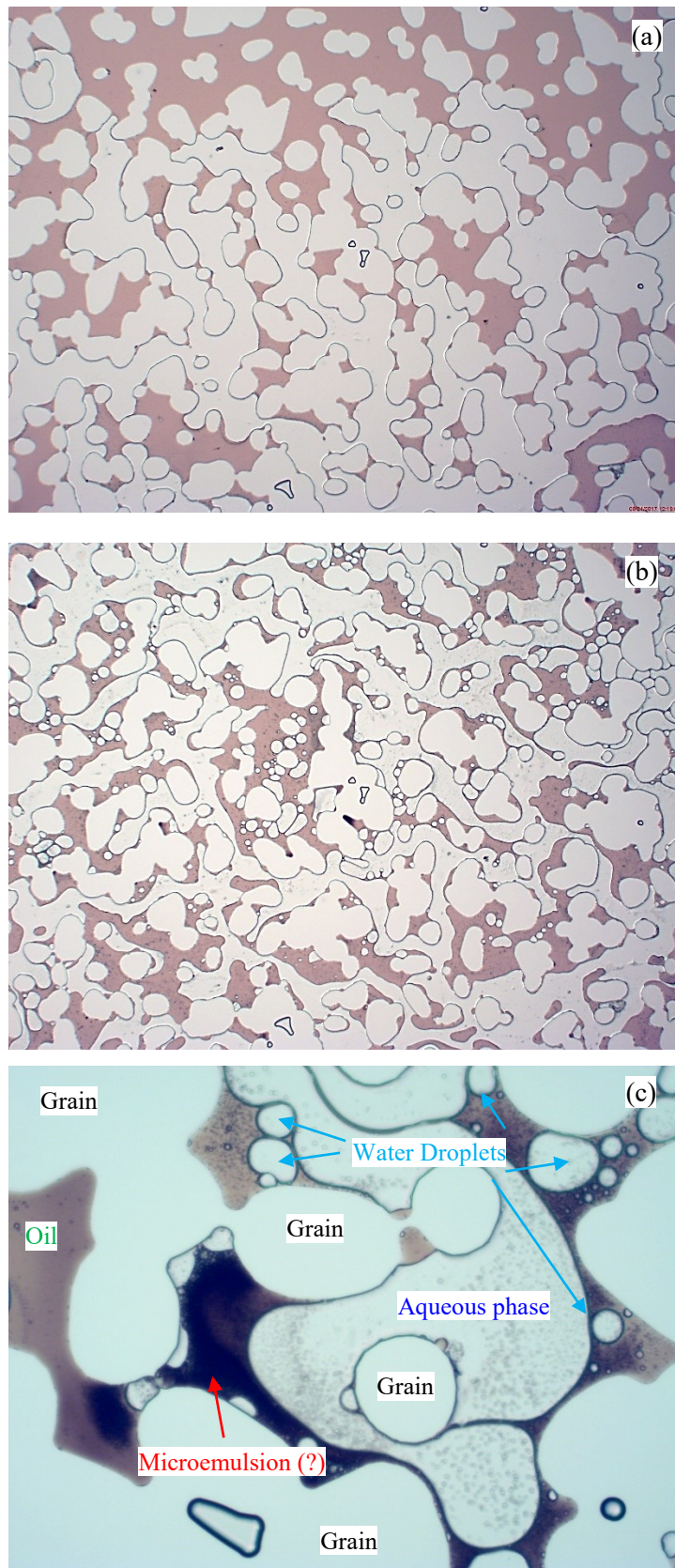
Figure 5-10 – Microscope taken images of experiment 15 (tertiary Na$_2$CO$_3$ solution injection into 8th TH oil sample), a) initial condition b) final condition c)W/O emulsion with different droplet sizes.
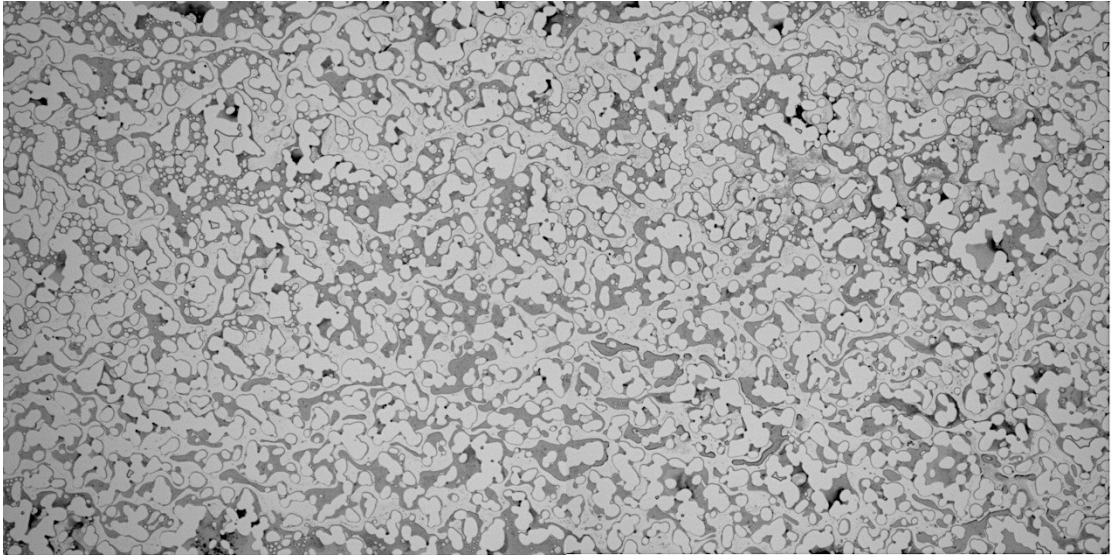
Figure 5-11 – Full range image of experiment 15 showing oil phase elongations and W/O emulsion
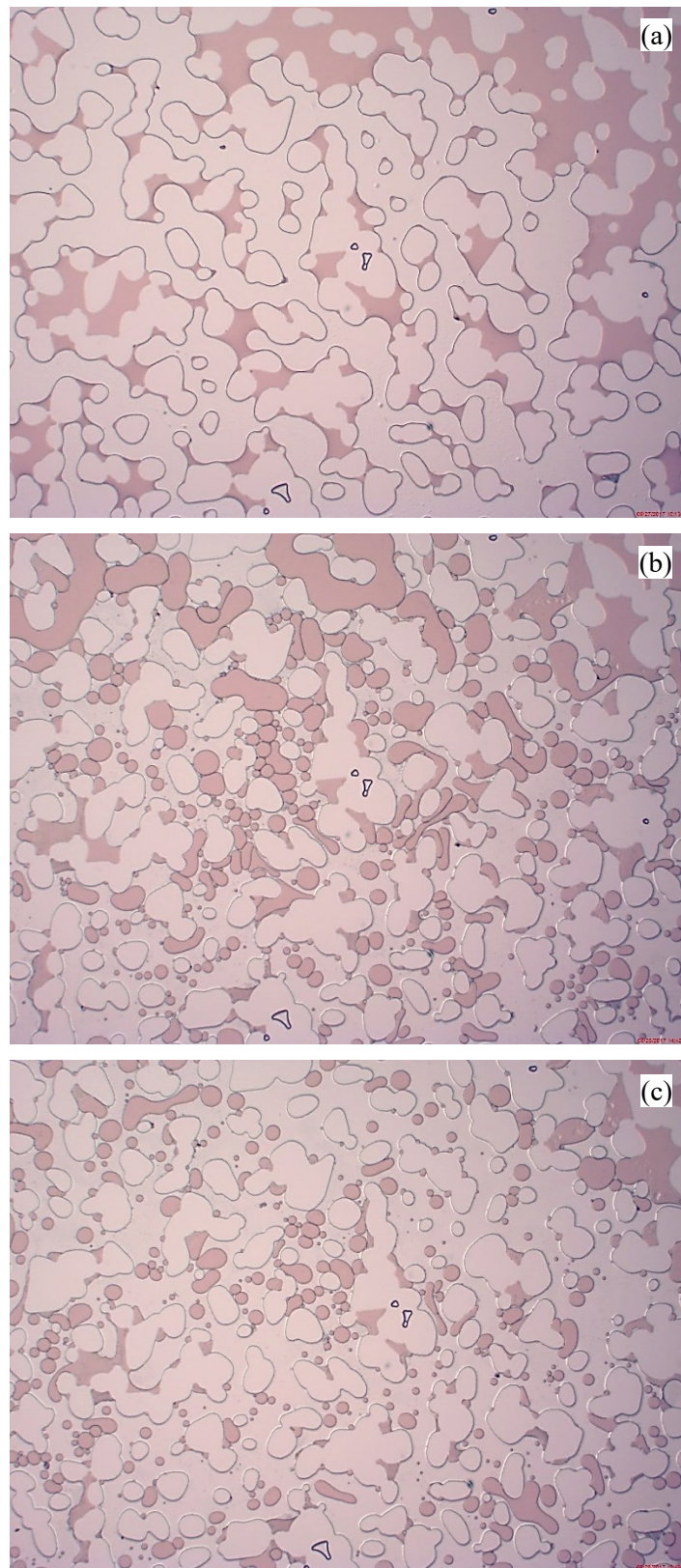
Figure 5-12 – Experiment 16 shows significant amount of oil droplets in aqueous phase, a)initial condition b) during the experiment c) final image taken when the injection has been stopped.

Figure 5-13 – Full range image of experiment 16 at final condition

5.2　Oil Recovery and Oil Saturation Curves

As previously stated and shown in Figure 4-8, microscopic images cover only 12% (24.4 mm^2) of the total area (200 mm^2) of microchip. This raises the question whether these microscope taken images can be considered as representative areas of the whole microchip in terms of porosity and fluid saturation measurements. To answer this question, representative elementary area (REA) for porosity and fluid saturations had to be determined. By definition, REA is the smallest area over which a measu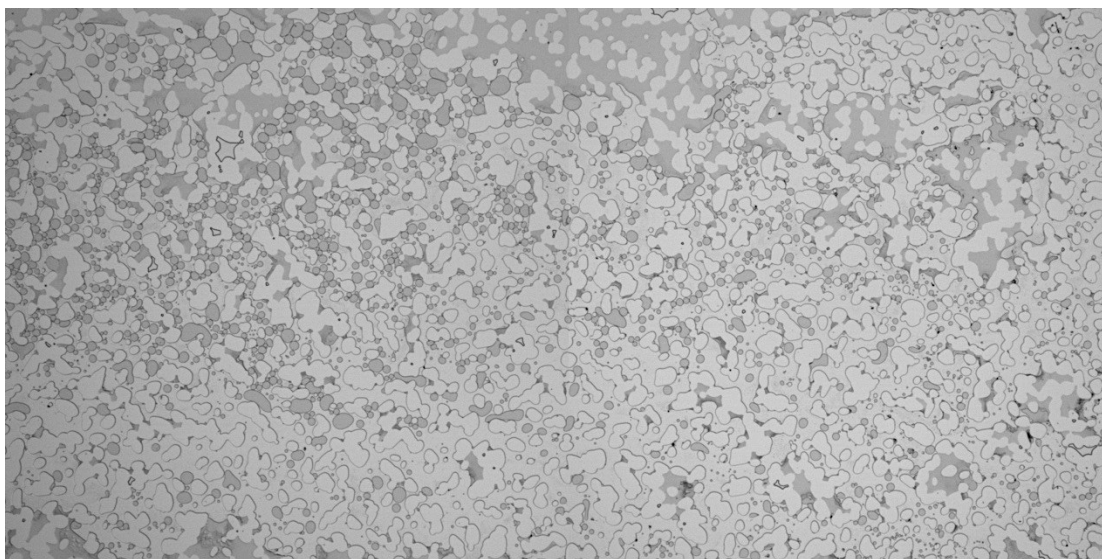rement (e.g. areal porosity and areal fluid saturation) can be made that will yield a representative value of the whole. In order to determine the REA for porosity and fluid saturation, these parameters were measured over a wide range of sample (area) sizes. For porosity, the full range image of the 100% oil saturated image was used. Porosity was measured over an area range from 54 mm^2 to 1 mm^2. For each area size, 3-5 measurements were performed by changing the location of measurement area. Finally, by plotting the area size versus measured porosity the REA could be determined. As shown in Figure 5-14, the red dotted line represents the actual porosity of 62.5% that was calculated over the whole range of microchip. The blue line represents the values of measured porosity over the sample areas. Error bars show 3% deviation from the reference value. As it can be seen, out of range (3%) oscillations in measured porosity start for sample areas with the size of 15 mm^2 and above this size, measured porosity values show an error of less than 3%. One may then conclude that the REA for porosity is 15 mm^2, therefore, the area which is covered by the microscope can be considered as a representative area with respect to porosity.
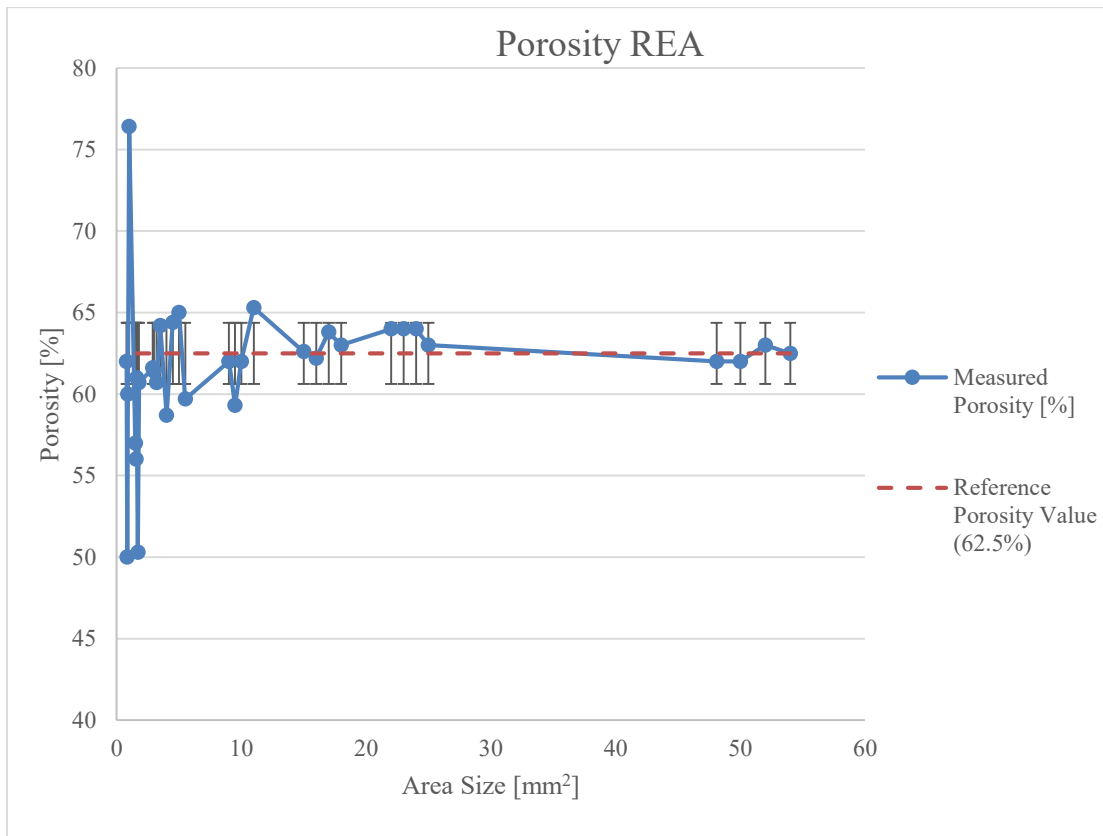
Figure 5-14 – REA determination plot for porosity.

Same measurements were performed for fluid saturations using a number of full range images. Generally, as the heterogeneity of fluid saturation distribution (either at ultimate condition or during the displacement process) is significant, no fluid saturation REA has been detected. As an example, Figure 5-15 shows the fluid saturation REA analysis that was performed based on the ultimate full range image of experiment 10. Red dotted line represents the reference oil saturation (0.54) measured over the full range image at final condition of experiment 10. Error bars show 3% deviation from the reference value. In this case, oscillations for the obtained oil saturation were still significant at sample area of 100 mm². This concludes that the area covered by the microscope cannot be considered as a REA of the microchip sample.
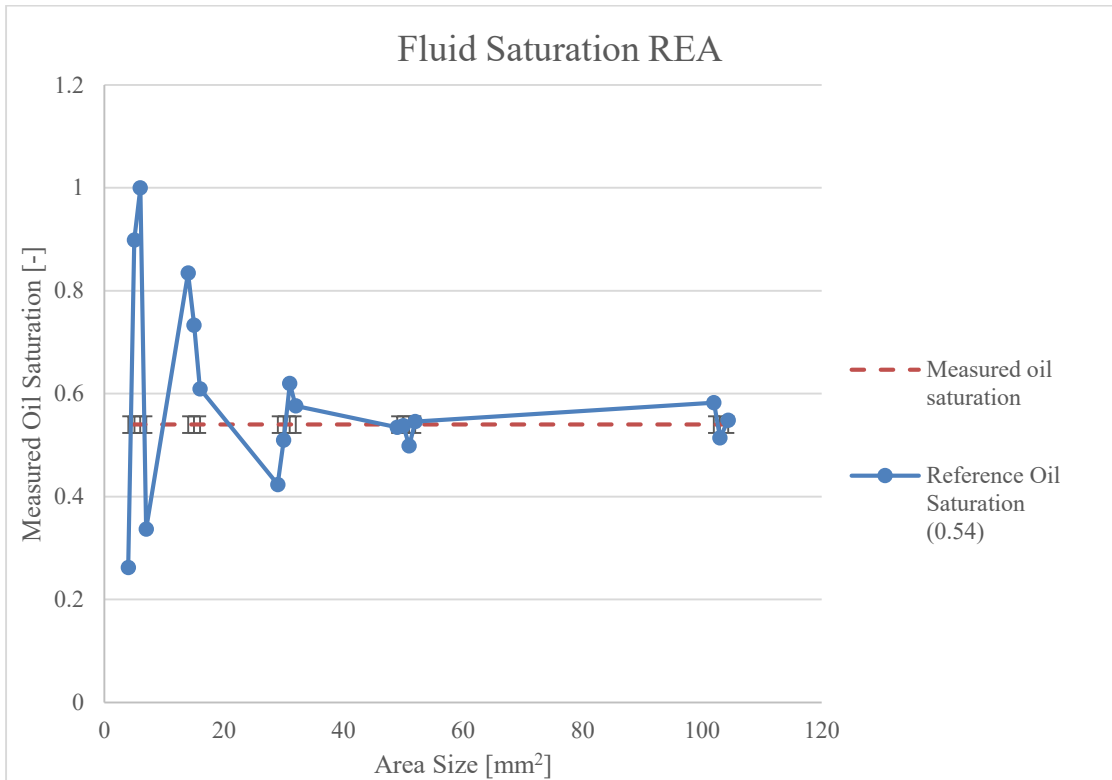
Figure 5-15 – REA determination for oil saturation

Oil recovery and oil saturation curves based on microscope taken images are plotted and presented for alkaline experiments in which recovery enhancement was observed (Figure 5-16 to Figure 5-19).

The graph in Figure 5-16 illustrates that secondary alkaline solution injection yielded higher recovery for 8th TH oil sample compared to the 16th TH that may be related to the higher TAN of the former oil sample. It is also clear that the injection of Na_2CO_3 solution resulted in higher recovery compared to the NaOH solution with the same alkalinity, whereas the NaOH solution had higher pH rather than the Na_2CO_3 solution. Furthermore, even by injecting small volumes of Na_2CO_3, the ultimate recovery was reached. Same results can be seen in the tertiary alkaline solution injection experiments (Figure 5-17). Note that in Figure 5-17, relative tertiary oil recovery is plotted versus injected pore volume.

Figure 5-16 – Oil recovery curves obtained from secondary alkaline flooding scenarios

Figure 5-17 – Oil recovery curves obtained from tertiary alkaline flooding scenarios.

Figure 5-18 – Oil saturation curves obtained from secondary alkaline flooding scenarios
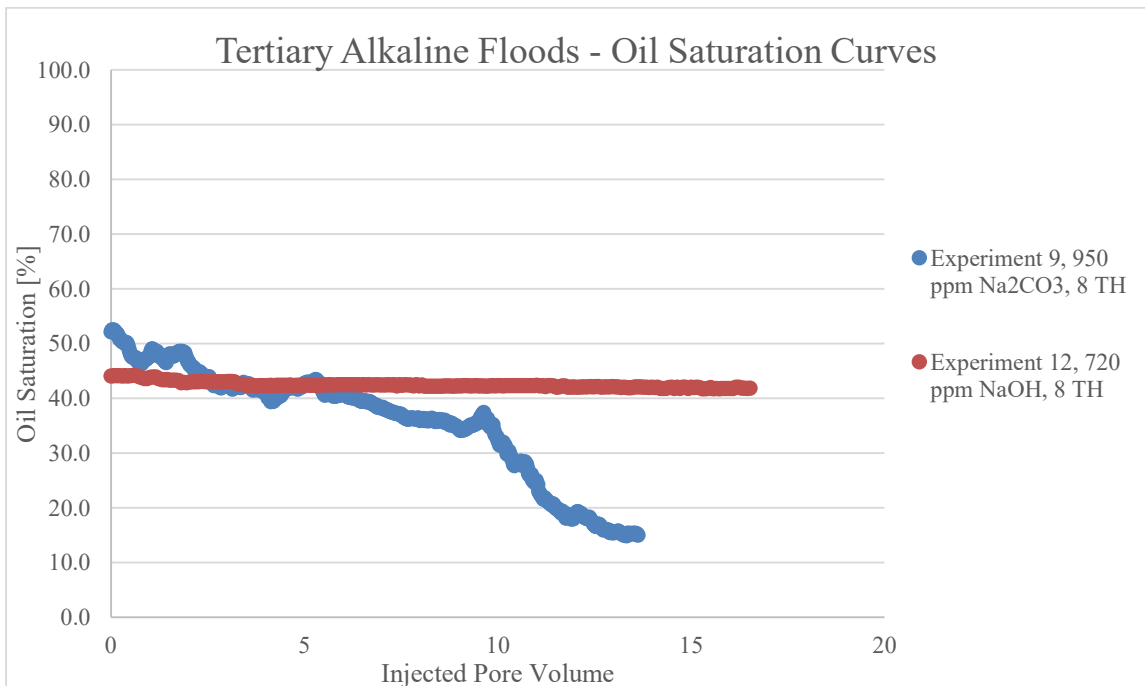
Figure 5-19 – Oil saturation curves obtained from tertiary alkaline flooding scenarios
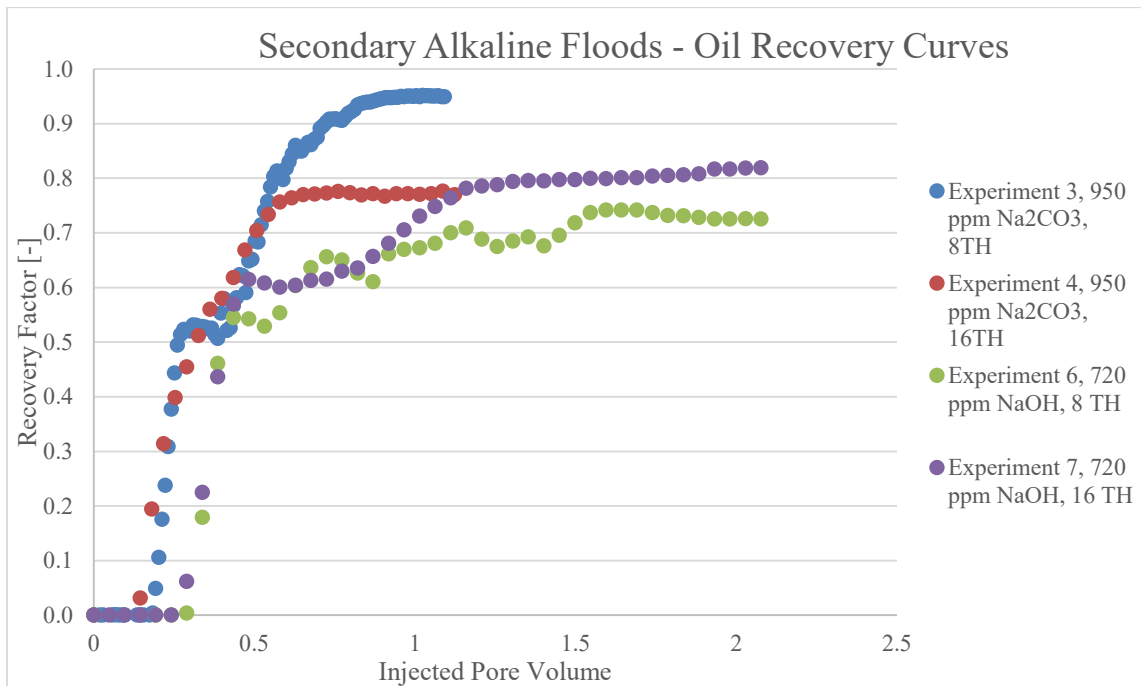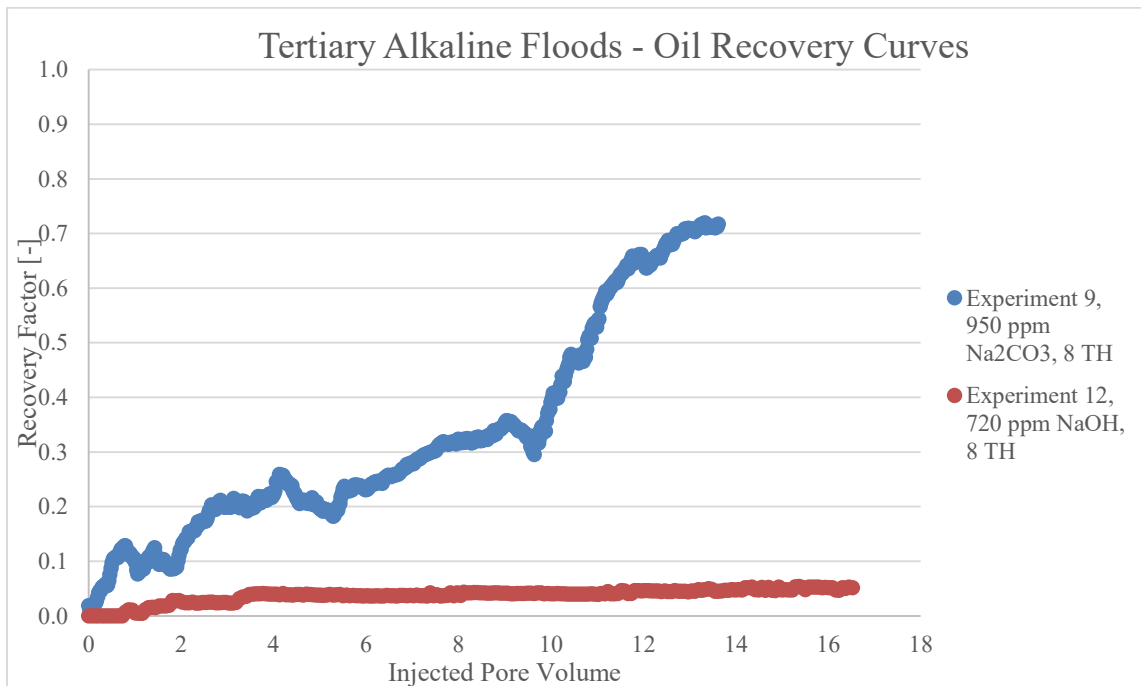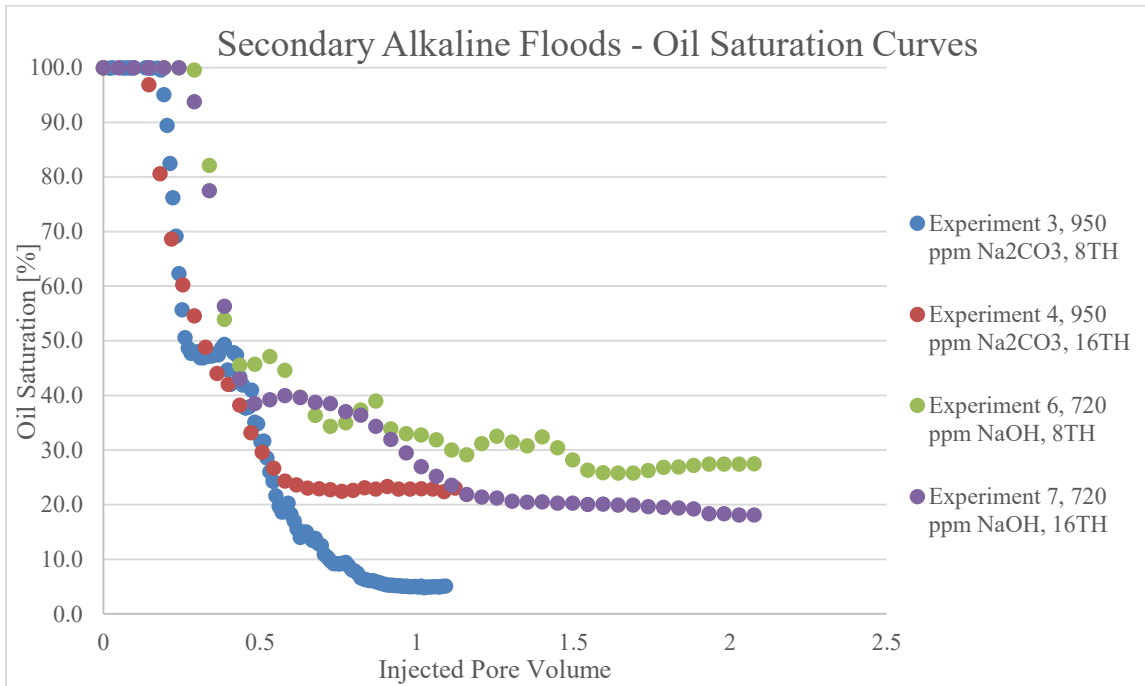
Chapter 6

Conclusions

6.1   Summary

This research was conducted to study the effect of alkaline solution flooding on oil recovery using microfluidic devices. Different experimental scenarios were designed and implemented to investigate the effect of influencing parameters such as:

- Oil type (different TANs and compositions)
- Alkaline type (sodium carbonate and sodium hydroxide)
- Alkaline concentration
- Secondary and tertiary flooding mode

Highest recoveries were achieved when alkaline solutions flooded high TAN oil samples (8th TH and 16th TH). Oil threads and elongated clusters were observed that might be related to low interfacial tension as a result of in-situ soap generation. The oil sample with low TAN (Flysch) showed no recovery enhancement by alkaline flooding.

Experiments proved that alkaline solution – crude oil interactions are highly dependent on alkaline types. Lower concentrations of sodium carbonate solution showed higher oil recoveries compared to the use of sodium hydroxide solution that can be interpreted as the important role of salinity. It is worth mentioning that higher pH values were recorded for NaOH solutions compared to sodium carbonate solutions.

The range of effective alkaline concentration must be investigated. As observed in this thesis, this range is not fixed and has to be studied separately for different oil types. For instance, injecting a 950 ppm sodium carbonate solution in 8th TH oil sample resulted in higher recovery compared to injection of a 12000 ppm sodium carbonate solution, whereas the opposite effects

were observed for the 16th TH oil sample. O/W and W/O emulsion formation occurred depending on the concentration of alkaline solution and oil type.

Oil droplets in water aggregated next to each other but no coalescence has been observed.

In general, much lower ultimate residual oil saturations in secondary alkaline injection experiments under similar conditions (e.g. temperature, injection rate, etc.) were measured in contrast to tertiary flood experiments where the microchip was first flooded with water followed by an alkaline solution injection.

6.2   Future Work

The impact of many other influencing parameters on alkaline flooding processes such as salinity, brine composition, temperature, etc. can be investigated.

Furthermore, cluster sizes, fluid topology and capillary desaturation analysis with respect to microscopic and macroscopic capillary numbers can also be performed as future works.

For further investigations and focusing on specific mechanisms, special porous media patterns can be designed and manufactured.

In the scope of this thesis, only one inlet channel was available in the microchips. This means, injection of oil (when saturating the microchip) and alkaline solution was done using the same inlet tube, which yields alkaline consumption in the inlet tube before the solution reaches the porous media. In addition, during the water or alkaline injection experiments, remaining oil in the tubes may become mobilized and enter the microchip. Since the inlet tube has a large volume compared to the volume of microchips, the secondary mobilization of oil causes significant recovery calculation errors. Hence, providing a double inlet microchip is recommended.

As previously mentioned, the employed microscope has a limited range of view that cannot be considered as a representative area for fluid saturation determination. Using microscopes or optical devices with wider field of view can provide better monitoring of the microfluidic experiments.

References

Abrams, A. (1975): The influence of Fluid Viscosity, Interfacial Tension and Flow Velocity on Residual Oil Saturation Left by Waterflood. In *SPEJ* Oct., pp. 437–447.

amrita.olabs.edu.in (2013): Saponification-The process of Making Soap. Available online at amrita.olabs.edu.in/?sub=73&brch=3&sim=119&cnt=1, checked on 3/20/2017.

Armstrong, Ryan T.; Georgiadis, Apostolos; Ott, Holger; Klemin, Denis; Berg, Steffen (2014): Critical capillary number. Desaturation studied with fast X-ray computed microtomography. In *Geophys. Res. Lett.* 41 (1), pp. 55–60. DOI: 10.1002/2013GL058075.

Biolin Scientific: Critical Micelle Concentraion. Available online at http://www.biolinscientific.com/zafepress.php?url=%2Fpdf%2FAttension%2FTheory%20Notes%2FAT-TN-03-Critical-micelle-concentration.pdf.

Bunge, A. L.; Radke, C. J. (1982): Migration of alkaline pulses in reservoir sands. SPEJ, December: 998–1012.

Burk, J. H. (1987): Comparison of sodium carbonate, sodium hydroxide, and sodium orthosilicate for EOR. In *SPERE (February)*, pp. 9–16.

Campell, T. C. (1982): The role of alkaline chemicals in the recovery of low-gravity crude oils. In *JPT (November)*, pp. 2510–2516.

Castor, T. P.; Somerton, W. H.; Kelly, J. F. (1981b): Recovery mechanisms of alkaline flooding. In: Shah, D.O. (Ed.), Surface Phenomena in Enhanced Oil Recovery. Plenum, pp. 249–291.

Cheng, K. H. (1986): Chemical Consumption During Alkaline Flooding. A Comparative Evaluation. In : SPE Enhanced Oil Recovery Symposium. SPE Enhanced Oil Recovery Symposium. Tulsa, Oklahoma, 1986-04-20: Society of Petroleum Engineers.

Cooke, C. E.; Williams, R. E.; Kolodzie, P. A. (1974): Oil recovery by alkaline waterflooding. In *JPT (February)*, pp. 1365–1374.

deZabala, E. F.; Vislocky, J. M.; Rubin, E.; Radke, C. J. (1982): A chemical theory for linear alkaline flooding. SPEJ, April: 245–258.

Dullien, F. A. L. (1979): Porous Media: Fluid Transport and Pore Structure. In *Academic Press* 2nd edition.

Green, Don W.; Willhite, G. Paul (1998): Enhanced oil recovery. Richardson, Tex.: Society of Petroleum Engineers (SPE textbook series, v.6).

Hilfer, R.; Øren, P. E. (1996): Dimensional analysis of pore scale and field scale immiscible displacement. In *Transport in Porous Media* 22, pp. 53–72.

http://www.micronit.com. Edited by Micronit microtechnologies B.V. Available online at http://www.micronit.com/, checked on 4/14/2017.

ImageJ User Guide. Available online at https://imagej.nih.gov/ij/docs/guide/146-29.html, checked on June, 2017.

Jennings, H. Y.; Johnson, Jr., C. E.; McAuliffe, C. D. (1974): A Caustic Waterflooding Process for Heavy Oils. In *JPT (December)*, pp. 1344–1352.

Johnson, Jr., C. E. (1976): Status of caustic and emulsion methods. In *JPT (January)*, pp. 85–92.

Karadimitriou, N. K.; Hassanizadeh, S. M. (2012): A Review of Micromodels and Their Use in Two-Phase Flow Studies. In *Vadose Zone Journal* 11 (3), p. 0. DOI: 10.2136/vzj2011.0072.

Labrid, J. (1991): The use of alkaline agents in enhanced oil recovery processes. In *In: Bavière, M. (Ed.), Basic Concepts in Enhanced Oil Recovery Processes. Elsevier Science*, pp. 123–155.

Lake, Larry W. (2014): Fundamentals of enhanced oil recovery. Second edition. Richardson Texas: Society of Petroleum Engineers.

Leal, L. Gary (2007): Advanced transport phenomena. Fluid mechanics and convective transport processes / L. Gary Leal. Cambridge: Cambridge University Press (Cambridge

series in chemical engineering). Available online at
http://www.loc.gov/catdir/enhancements/fy0665/2006018348-d.html.

Mayer, E. H.; Berg, R. L.; Carmichael, J. D.; Weinbrandt, R. M. (1983): Alkaline injection for enhanced oil recovery–a status report. In *JPT (January)*, pp. 209–221.

Melrose, J. C.; Brandner, C. F. (1974): Role of Capillary Forces In Determining Microscopic Displacement Efficiency For Oil Recovery By Waterflooding. In *Journal of Canadian Petroleum Technology. DOI:* 10.2118/74-04-05.

Moore, T. F.; Slobod, R. C. (1956): The Effect of Viscosity and Capillarity on the Displacement of Oil by Water. In *Producers Monthly (August)*, pp. 20–30.

Mukerjee, P.; Mysels, K. J. (1971): Critical micelle concentrations of aqueous surfactant systems, NSRDS-NBS 36.

Mungan, N. (1966a): Certain wettability effects in laboratory waterfloods. In *JPT (February)*, pp. 247–252.

Mungan, N. (1966b): Interfacial effects in immiscible liquid-liquid displacement in porous medium. In *SPEJ (September)*, pp. 247–253.

Novosad, Z.; et al. (1981): Comparison of oil recovery potential of sodium orthosilicate and sodium hydroxide for the Wainwright reservoir, Alberta. In *Petroleum Recovery Institute Report* No. 81-10 (July).

Ramakrishnan, T. S.; Wasan, D. T. (1983): A Model for Interfacial Activity of Acidic Crude Oil/Caustic Systems for Alkaline Flooding. In *Society of Petroleum Engineers Journal* 23 (04), pp. 602–612. DOI: 10.2118/10716-PA.

Sheng, James (2011): Modern chemical enhanced oil recovery. Theory and practice / James Sheng. Amsterdam, Boston, Mass.: Gulf Professional Pub.

Sheng, James (Ed.) (2013): Enhanced oil recovery field case studies. Amsterdam: Gulf Professional Publishing.

Stumm, Werner; Morgan, James J. (1970): Aquatic Chemistry. Chemical Equilibria and Rates in Natural Waters: Wiley.

Subkow, P. (1942): Process for the removal of bitumen from bituminous deposits. In *US Patent No. 2,288,857, 7 July*.

Zhao, S.; Zhang, L.; Luo, L.; Yu, J. Y. (2002): Synergy between displacement agents and the active components of crude oils, In: Yu, J.-Y., Song, W.-C., Li, Z.-P., et al. (Eds.), Fundamentals and Advances in Combined Cehmical Flooding, Chapter 2. China Petrochemical Press.

Appendix A

Developed Macros for Image Analysis

Full-range Image Analysis

```
macro " Full-range Image Analysis" {

        dirS = getDirectory ("Choose Source Directory  ");

        Filename = getFileList (dirS);

        dirD = getDirectory ("Choose Destination Directory  ");

        for (i=0; i<Filename.length; i++) {

                open(dirS + Filename[i]);

                run("Subtract Background...", "rolling=50 light");

                run("Split Channels");

                selectWindow(Filename[i] + " (blue)");

                setAutoThreshold("Default dark");

                //run("Threshold...");

                setThreshold(247,255);

                setOption("BlackBackground", true);

                run("Convert to Mask");

                run("Dilate");

                run("Dilate");

                run("Erode");

                run("Erode");
```

```
        run("Invert");

        run("Measure");

        AreaPercent = getResult("%Area", i);

        print ( Filename[i], "          ", AreaPercent) ;

        FilenameProcessed = Filename[i] + "_Processed";

        saveAs ("bmp", dirD + FilenameProcessed);

        close();

        selectWindow(Filename[i] + " (green)");

        close();

        selectWindow(Filename[i] + " (red)");

        close();

        }

}
```

Microscope-taken Image Analysis

```
macro " Microscope-Taken Image Analysis" {

        dirS = getDirectory ("Choose Source Directory  ");

        Filename = getFileList (dirS);

        dirD = getDirectory ("Choose Destination Directory  ");

        for (i=0; i<Filename.length; i++) {

                open(dirS + Filename[i]);

                run("8-bit");

                run("Subtract Background...", "rolling=250 light");

                selectWindow(Filename[i]);

                setAutoThreshold("Default dark");

                //run("Threshold...");

                //setThreshold(237,255);
```

```
        setOption("BlackBackground", true);

        run("Convert to Mask");

        run("Dilate");

        run("Dilate");

        run("Erode");

        run("Erode");

        run("Invert");

        run("Measure");

        AreaPercent = getResult("%Area", i);

        print ( Filename[i], "          ", AreaPercent) ;

        FilenameProcessed = Filename[i] + "_Processed";

        saveAs ("bmp", dirD + FilenameProcessed);

        close();

        }

}
```